Army Research Laboratory
Aberdeen Proving Ground, MD 21005-5066

ARL-TR-2589 December 2001

Numerical Computations of Supersonic Flow Over Elliptical Projectiles

Jubaraj Sahu
Karen R. Heavey
Harris L. Edge
Weapons and Materials Research Directorate

Approved for public release; distribution is unlimited.

Abstract

Computational fluid dynamics (CFD) approaches were used to compute the supersonic and hypersonic flow fields and aerodynamic forces and moments on elliptical projectiles. Steady state numerical results have been obtained at several supersonic Mach numbers between 2.5 and 4.0 and several angles of attack from 0 to 12 degrees for the "jet-off" conditions with the use of Euler and Navier-Stokes flow solvers. In addition, numerical computations have been performed for the "jet-on" conditions to study the interaction of a helium jet with a free stream Mach 4.0 flow. In general, very good agreement of the computed aerodynamic coefficients with the experimental data was achieved at all speeds and angles of attack investigated for jet-off conditions. A small discrepancy exists in the comparisons for the axial force. CFD results for the jet-on case show the qualitative features and strong flow interaction between the jet and the free stream flow. The results show the predictive capabilities of CFD techniques for supersonic flow over elliptical projectiles.

ACKNOWLEDGMENTS

The authors wish to thank D.M. Orchard, Qinetiq, United Kingdom (UK), E. Fournier, Defence Research Establishment, Valcartier, Canada, J.A. Edwards, Defence Evaluation and Research Agency, UK, for all their help in providing the experimental data to validate the computed results. Special thanks to D.M. Orchard for all the discussions about and assistance in analyzing the data. The authors wish to thank S.R. Chakravarthy of Metacomp Technologies and his colleagues for all their help with the application of the CFD++ code to our problem. The scientific visualization work of R. Angelini of the U.S. Army Research Laboratory (ARL) and the computational support of the ARL major shared resource center are greatly appreciated.

INTENTIONALLY LEFT BLANK

Contents

1. **Introduction** 1

2. **Solution Technique** 2
   2.1 Euler Zeus GUI Code 2
   2.2 ZNSFLOW Solver 3
   2.3 Governing Equations 4
   2.4 Numerical Algorithm 4
   2.5 CFD++ Flow Solver 5

3. **Chimera Composite Grid Scheme** 7

4. **Model Geometry and Computational Grid** 7
   4.1 Zeus Computational Mesh 7
   4.2 Navier-Stokes Computational Meshes 8

5. **Results** 13
   5.1 Zeus Euler Code Results (jet off) 13
   5.2 Navier-Stokes Results (jet off) 17
   5.3 Jet-On Results 25

6. **Conclusion** 30

References 31

Distribution List 35

Report Documentation Page 39

Figures

1. Zeus GUI 3
2. H3P78 Projectile 9
3. Full Grid for Viscous Computations, Jet Off 9
4. Expanded View of the Grid in the Base Region, Jet Off 10
5. Circumferential Cross Section of the Grid at the Base 10
6. Full Grid for Viscous Computations, Jet On 11
7. Expanded View of the Grid in the Base Region, Jet On 12
8. Expanded View of the Jet Grids Projected Onto the Projectile Surface 12
9. Pressure Contours, $M = 4$, $\alpha = 4°$ 13
10. Pressure Contours, $M = 4$, $\alpha = 8°$ 14
11. Pressure Contours, $M = 4$, $\alpha = 12°$ 14
12. Angle Force Versus Angle of Attack 15
13. Normal Force Versus Angle of Attack 15
14. Pitching Moment Versus Angle of Attack 16
15. Force/Moment Versus Body Length 16

16. Computed Pressure Contours, M = 2.5, α = 4°, 8°, 12° 19
17. Computed Pressure Contours, M = 4.0, α = 4°, 8°, 12° 20
18. Computed Particle Traces, M = 4, α = 12 21
19. Normal Force Coefficient, M = 2.5 21
20. Pitching Moment Coefficient, M = 2.5 22
21. Axial Force Coefficient, M = 2.5 22
22. Normal Force Coefficient, M = 4.0 23
23. Pitching Moment Coefficient, M = 4.0 23
24. Axial Force Coefficient, M = 4.0 24
25. Effects of Turbulence on Axial Force Coefficient, M = 4.0 24
26. H3P78 Projectile, Showing the Jet Locations 25
27. Computed Pressure Contours, Jet On, 100% Jet Pressure, M = 4.0, α = 0° 25
28. Computed Pressure Contours Near the Jet and Wake, Jet On, 100% Jet Pressure, M = 4.0, α = 0° 26
29. Computed Surface Pressure Contours Near the Jet, 50% Jet Pressure, M = 4.0, α = 0° 27
30. Computed Helium Concentration Contours Near the Base Region, (a) 100%, (b) 50%, and (c) 25% Jet Pressures, M = 4.0, α = 0° 28
31. Surface Pressure Contours Comparison Along the Centerline of Symmetry, M = 4.0, α = 0° 29
32. Surface Pressure Contours Comparison Along the Centerline of Jet, M = 4.0, α = 0° 29

NUMERICAL COMPUTATIONS OF SUPERSONIC FLOW
OVER ELLIPTICAL PROJECTILES

1. Introduction

The advancement of computational fluid dynamics (CFD) has had a major impact on projectile design and development [1,2,3,4]. Improved computer technology and state-of-the-art numerical procedures enable solutions to complex, three-dimensional (3-D) problems associated with projectile and missile aerodynamics. In general, these techniques produce accurate and reliable numerical results for projectiles and missiles at small angles of attack. Modern projectiles and missiles are expected to experience moderate to large angles of attack during flight. Of particular interest is the accurate determination of supersonic and hypersonic flow over elliptical projectiles at moderate angles of attack. The flow field for such projectiles with non-axisymmetric cross sections is complex, especially in the presence of jets used to maneuver these projectiles. The work presented in this report was initiated as part of The Technical Cooperation Program (TTCP) effort with participants from Canada, the United Kingdom, and the United States and was aimed at assessing the capabilities of the both Euler and Navier-Stokes solvers currently available to research scientists for supersonic and hypersonic flow over elliptical projectiles for both "jet-off" and "jet-on" conditions [5]. The TTCP research effort has also focused on the wind tunnel testing as well as free flight testing of these projectiles. Different aspects of computational techniques, such as grid generation, algorithms, turbulence modeling and flow field visualization, have been addressed by the group.

Inviscid solutions were obtained for H-series projectiles with the use of the Euler Zeus graphical user interface (GUI) code [6,7]. Computations of the H3 projectile and its variations (with and without flares and strakes) were performed with the Euler Zeus code at M = 8.2 and several angles of attack between 0° and 15°. Comparison was made of stabilization by strakes and flare for a different H-series projectile [8]. The computations indicated that although the flare gave increased drag, it was still substantially more effective in providing stability than strakes alone. The present research focuses on the application of CFD techniques for accurate numerical prediction of supersonic flow over the elliptical H3P78 projectile. Calculations for the H3P78 projectile were performed with the Zeus Euler code and two Navier-Stokes flow solvers: the zonal Navier-Stokes flow (solver) (ZNSFLOW) [9] and CFD++ [10,11], at several supersonic Mach numbers between 2.5 and 4.0 and several angles of attack from 0° to 12° for the jet-off conditions. In addition, numerical computations for the H3P78 projectile have been performed for the jet-on conditions with the CFD++ code to study the interaction of a helium jet with a free stream M = 4.0 flow.

A description of the computational techniques is presented, followed by a description of the applications of these techniques to the H3P78 projectile. Results for this configuration are shown at various supersonic speeds and angles of attack. Computed data have been compared with experimental data provided by the Defence Evaluation and Research Agency (DERA), United Kingdom (UK) **[5]** and obtained at the Defence Research Establishment, Valcartier (DREV), Canada **[12]**.

2. Solution Technique

2.1 Euler Zeus GUI Code

Development of the Zeus GUI code **[6,7]** at the U.S. Army Research Laboratory (ARL) was undertaken at the request of the Aviation and Missile Research Development and Engineering Center (AMRDEC) and was funded by ARL as part of a Technology Program Annex (TPA) agreement. A picture of the Zeus GUI code in use is shown in Figure 1. As a starting point for this effort, the zonal Euler solver or Zeus code **[13,14]** was chosen by AMRDEC to be incorporated into a GUI environment. The original Zeus code was developed by the Navy and is widely used within the international missile design community. Zeus is a zonal Euler CFD solver, which employs a second order Godunov scheme to integrate the Euler equations and march the solution longitudinally along the body. The solver algorithm in the ARL Zeus GUI is identical to the one implemented in the original Zeus code. One can obtain additional details about the integration scheme by referring to the work of Wardlaw **[13,14]**.

In terms of the application of Zeus, there are some restrictions of its use. First, Zeus can only be applied to cases in which the entire flow field is supersonic. Zeus employs the Euler equations and therefore is most suitable for cases in which the boundary layer is assumed to be thin and its effects can be neglected. The computational mesh should be free of blunt discontinuities. Auxiliary programs are available to generate Zeus-compatible solution planes for blunt noses when the computational mesh is not compatible with Zeus topology and when subsonic flow may occur. Zeus was written to support a zonal grid topology. The zonal topology allows fins or wings to be modeled. However, the leading and trailing edges should be fairly sharp.

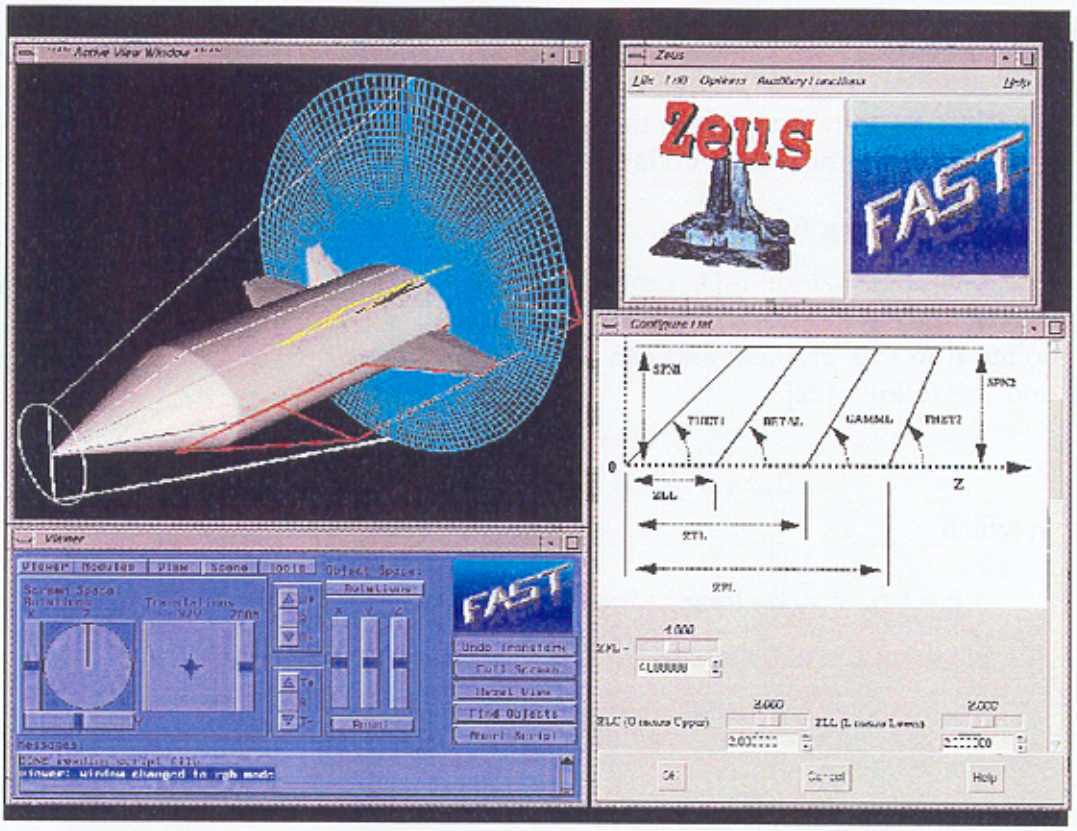

Figure 1. Zeus GUI.

2.2 ZNSFLOW Solver

The ZNSFLOW solver is a product of a common high performance computing software support initiative (CHSSI) project [9]. It is a descendant of F3D [16], a code used successfully for many years on Cray vector processors such as the C90. Under CHSSI, it was rewritten to provide scalable performance on a number of computer architectures. Programming enhancements include the use of dynamic memory allocation and highly optimized cache management. ZNSFLOW features a GUI to facilitate problem setup. It has been used extensively in the computation of flow field calculations for projectile and missile programs of interest to the U.S. Army [1,2,3,4,9,15]. The flow solver includes the chimera [17,18,19] overset discretization technique for CFD modeling of complex configurations. By using the chimera technique, one can greatly simplify the grid topology and grid generation for very complex systems. One of the disadvantages in using the chimera technique has been the increased complexity and corresponding confusion in the application of a turbulence model. A chimera model can be composed of multiple zones, with each zone possibly having a unique grid topology. Most turbulence models have specific direction-, orientation-, or distance-related requirements for correct application. For a complex chimera model, applying a turbulence model can be a very complex process, especially an algebraic model such as Baldwin-Lomax [20] model. We

have addressed this problem in ZNSFLOW by installing point-wise one- and two-equation turbulence models **[21]** that are not orientation specific. This greatly simplifies the setup of the turbulence model. Wall location information is supplied when the wall boundary conditions are set by the user.

2.3 Governing Equations

The complete set of 3-D, time-dependent, generalized geometry, Reynolds-averaged, thin layer Navier-Stokes equations is solved numerically to obtain a solution to this problem and can be written in general spatial coordinates ξ, η, and ζ as follows **[22]**:

$$\partial_\tau \hat{q} + \partial_\xi \hat{F} + \partial_\eta \hat{G} + \partial_\zeta \hat{H} = \mathrm{Re}^{-1}\, \partial_\zeta \hat{S}, \tag{1}$$

in which

$\xi = \xi$ (x, y, z, t) - longitudinal coordinate,

$\eta = \eta$ (x, y, z, t) - circumferential coordinate,

$\zeta = \zeta$ (x, y, z, t) - nearly normal coordinate, and

τ = t - time.

In Equation 1, $\hat{q}$ contains the dependent variables (density, three velocity components, and energy), and $\hat{F}$, $\hat{G}$, and $\hat{H}$ are flux vectors. The thin layer approximation is used here, and the viscous terms involving velocity gradients in both the longitudinal and circumferential directions are neglected. The viscous terms are retained in the normal direction, ζ, and are collected into the vector, $\hat{S}$. In the wake or the base region, similar viscous terms **[1]** are also added in the streamwise direction, ξ. An implicit, approximately factored scheme is used to solve these equations. For the computation of turbulent flows, the turbulent contributions are supplied through an algebraic eddy viscosity turbulence model developed by Baldwin and Lomax **[20]** or a point-wise turbulence model **[21]**.

2.4 Numerical Algorithm

The implicit, approximately factored scheme for the thin layer Navier-Stokes equations with central differencing in the η and ζ directions and "upwinding" in ξ is written in the following form **[16]**:

$$\begin{aligned}
&\left[\, I + i_b h\, \delta_\xi^{\mathrm{b}}\, (\hat{A}^+)^n + i_b h\, \delta_\zeta \hat{C}^n - i_b h\, \mathrm{Re}^{-1}\, \bar{\delta}_\zeta\, J^{-1}\, \hat{M}^n J - i_b D_i\, |_\zeta \,\right] \\
&\times [\, I + i_b h\, \delta_\xi^{\mathrm{f}}\, (\hat{A}^-)^n + i_b h\, \delta_\eta \hat{B}^n - i_b D_i\, |_\eta \,]\, \Delta \hat{Q}^n \\
&= i_b\, \Delta t\, \{\, \delta_\xi^{\mathrm{b}}\, [\, (\hat{F}^+)^n - \hat{F}_\infty^- \,] + \delta_\xi^{\mathrm{f}}\, [\, (\hat{F}^-)^n - \hat{F}_{-\infty}^- \,] + \delta_\eta\, (\hat{G}^n - \hat{G}_\infty) \\
&+ \delta_\zeta\, (\hat{H}^n - \hat{H}_\infty) - \mathrm{Re}^{-1}\, \bar{\delta}_\zeta\, (\hat{S}^n - \hat{S}_\infty)\, \} - i_b D_e (\hat{Q}^n - \hat{Q}_\infty)\,,
\end{aligned} \tag{2}$$

in which $h = \Delta t$ or $(\Delta t)/2$ and the free stream base solution is used. The free stream fluxes are subtracted from the governing equation to reduce the possibility of error from the free stream solution, which corrupts the converged solution. Here, δ is typically a three-point second order accurate central difference operator, $\bar{\delta}$ is a midpoint operator used with the viscous terms, and the operators δ_ξ^{b} and δ_ξ^{f} are backward and forward three-point difference operators. The flux $\hat{F}$ has been eigensplit, and the matrices $\hat{A}, \hat{B}, \hat{C}$, and $\hat{M}$ result from local linearization of the fluxes about the previous time level. Here, J denotes the Jacobian of the coordinate transformation. Dissipation operators D_e and D_i are used in the central space-differencing directions. The smoothing terms used in the present study are of the form

and

$$D_e|_\eta = (\Delta t)\, J^{-1} \left[\varepsilon_2\, \bar{\delta}\rho(B)\, \beta\, \bar{\delta} + \varepsilon_4 \bar{\delta}\, \frac{\rho(B)}{1+\beta}\, \bar{\delta}^{\,3} \right] |_\eta\, J,$$

$$D_i|_\eta = (\Delta t)\, J^{-1} \left[\varepsilon_2 \bar{\delta}\, \rho(B)\, \beta\, \bar{\delta} + 2.5\, \varepsilon_4 \bar{\delta}\rho(B)\bar{\delta} \right] |_\eta\, J, \tag{3}$$

in which

$$\beta = \frac{|\bar{\delta}^2 P|}{|(1+\delta^2)\, P|}, \tag{4}$$

and in which $\rho(B)$ is the true spectral radius of B. The idea here is that the fourth difference will be tuned down near shocks (e.g., as β gets large, the weight on the fourth difference drops down while the second difference tunes up).

2.5 CFD++ Flow Solver

The basic numerical framework in which the proposed scheme is implemented is termed the unified grid, unified physics and unified computing framework. These have been implemented in a software suite called CFD++ **[10,11]** and the user is referred to these references for details of the basic numerical framework. Here, only a brief synopsis of this framework and methodology is given.

The 3-D, time-dependent Reynolds-averaged Navier-Stokes (RANS) equations are solved by the finite volume method:

$$\frac{\partial}{\partial t}\int_V \mathbf{W}\, dV + \oint [\mathbf{F} - \mathbf{G}] \cdot dA = \int_V \mathbf{H}\, dV \tag{5}$$

in which **W** is the vector of conservative variables, **F** and **G** are the inviscid and viscous flux vectors, respectively, **H** is the vector of source terms, V is the cell volume, and A is the surface area of the cell face.

The numerical framework of CFD++ is based on the following general elements:

1. Unsteady compressible and incompressible Navier-Stokes equations with turbulence modeling [unified physics];

2. Unification of Cartesian, structured curvilinear, and unstructured grids, including hybrids [unified grid];

3. Unification of treatment of various cell shapes including hexahedral, tetrahedral, and triangular prism cells (3-d), quadrilateral and triangular cells (2-d), and linear elements (1-d) [unified grid];

4. Treatment of multi-block patched aligned (nodally connected), patched nonaligned and overset grids [unified grid];

5. Total variation diminishing discretization based on a new multi-dimensional interpolation framework;

6. Riemann solvers to provide proper signal propagation physics, including versions for preconditioned forms of the governing equations;

7. Consistent and accurate discretization of viscous terms via the same multi-dimensional polynomial framework;

8. Point-wise turbulence models that do not require knowledge of distance to walls;

9. Versatile boundary condition implementation includes a rich variety of integrated boundary condition types for the various sets of equations; and

10. Implementation on massively parallel computers based on the distributed memory message-passing model via native message-passing libraries or message-passing interface, parallel virtual machines, etc. [unified computing].

The code has assembled several ideas about convergence acceleration to yield a fast methodology for all flow regimes. The approach can be labeled as a "preconditioned implicit relaxation" scheme. It combines three basic ideas: implicit local time stepping, relaxation, and preconditioning. Preconditioning the equations ideally equalizes the eigenvalues of the inviscid flux Jacobians and removes the stiffness arising from large discrepancies between the flow and sound velocities at low speeds. The use of an implicit scheme circumvents the stringent stability limits suffered by their explicit counterparts, and successive relaxation allows cell revision as information becomes available and thus aids convergence.

The code has recently added the ability to handle multi-block meshes with various types of inter-block connectivities. Multi-dimensional interpolation more accurately represents local behavior of flow-dependent variables. While the formal order of accuracy does not need to be any higher, this approach leads to

practically higher accuracy on relatively coarse meshes. The multi-dimensional interpolation framework helps us to easily handle inter-block connectivities also. Second order discretization was used for the flow variables and the turbulent viscosity equation. The turbulence closure has been based on topology-parameter-free formulations. These models are ideally suited to unstructured bookkeeping and massively parallel processing because of their independence from constraints related to the placement of boundaries and/or zonal interfaces. Recent contributions to these models include (a) improved behavior of the dissipation rate transport equation by explicit sensitization to non-equilibrium flow regions, and (b) enhanced near-wall characteristics and elimination of *ad hoc* formulations through the introduction of time-scale realization.

3. Chimera Composite Grid Scheme

The chimera overset grid technique greatly adds to the number of applications to which the ZNSFLOW and CFD++ solvers can be applied. The chimera overset grid technique, which is ideally suited to complex configurations and multi-body problems **[1,2,3,4,17,18,19]**, involves generating independent grids about each body or component and then oversetting them onto a base grid to form the complete model. An advantage of the overset grid technique is that it allows computational grids to be obtained for each body component separately and thus makes the grid generation process easier. Because each component grid is generated independently, portions of one grid may lie within a solid boundary contained within another grid. Such points lie outside the computational domain and are excluded from the solution process. Equation 2 has been modified for chimera overset grids by the introduction of the flag i_b to achieve just that. This i_b array accommodates the possibility of having arbitrary holes in the grid. The i_b array is defined so that $i_b = 1$ at normal grid points and $i_b = 0$ at hole points. Thus, when $i_b = 1$, Equation 2 becomes the standard scheme. The set of grid points that forms the border between the hole points and the normal field points is called inter-grid boundary points. We revise these points by interpolating the solution from the overset grid that created the hole. Values of the i_b array and the interpolation coefficients needed for this revision are provided by a separate algorithm **[17]**.

4. Model Geometry and Computational Grid

4.1 Zeus Computational Mesh

One of the more convenient features of the Zeus GUI is the automatic grid generation. The user merely specifies the missile surface geometry, and the flow

field mesh is built plane by plane as the solution is computed. The current set of GUI-directed geometry input is capable of describing axisymmetric finned missiles. Since H-series projectiles are not axisymmetric, the projectile surface was generated by an auxiliary program and written as a set of discrete points to a file. The projectile surface was read into Zeus GUI via the user-defined surface option. The Zeus GUI also provides controls for mesh clustering. The mesh was clustered in the direction normal to the body at the surface. Pitch-plane symmetry was used for most computations. When pitch-plane symmetry was employed, 72 points were used in the circumferential direction. The outer grid boundary of the automatically generated grid is shock fitted. Therefore, the distance from the projectile body surface to the outer grid body grows as the solution is marched from nose to tail. In most cases, 36 points were used in the normal direction for the first 15% of body length; then the solution was stopped. The flow field solution for the remaining body length was usually computed with 72 points in the direction normal to the body, but for some high angle-of-attack cases, 120 points were used. To increase the number of points in the normal direction, an auxiliary program was used to interpolate a solution plane with 36 normal points to one with 72 normal points. The auxiliary program is accessible through the GUI and uses the GUI parameters, such as mesh cluster controls, to easily refine the computational mesh. At this mesh resolution, Zeus usually required approximately 5,000 axial planes to obtain the solution for the entire body length. A solution could be obtained with approximately 20 minutes of computer time on a Silicon Graphics workstation.

4.2 Navier-Stokes Computational Meshes

For the jet-off cases that use the Navier-Stokes flow solvers, two multi-block grids were developed. These structured multi-block grids have one-to-one overlaps at the zonal boundaries. Both grids are two zone H-grids. The H3P78 projectile is shown in Figure 2. The initial grid (GRID-1) used for these computations was a two-zone grid (see Figure 3) that consisted of 1.8 million grid points. Zone 1 grid along the projectile body, has 251 longitudinal points, 59 normal points, and 91 circumferential points, with an H-type grid at the nose of the projectile. The base grid, Zone 2, is an H-grid consisting of 50 longitudinal points, 113 normal points, and 91 circumferential points. The minimum spacing at the wall is 6.0E-05 mm (1E-06 calibers). An expanded view of the base region grid is shown in Figure 4.

Consisting of one million points, GRID-2 contains fewer total points but has a larger number of points (121 points, see Figure 5) in the circumferential direction in both zones. Zone 1 has 101 longitudinal points and 45 normal points, while Zone 2, in the wake region, has 40 longitudinal points and 99 normal points. The minimum spacing at the projectile wall is 2.0E-03 mm (3.0E-05 calibers) for both grids.

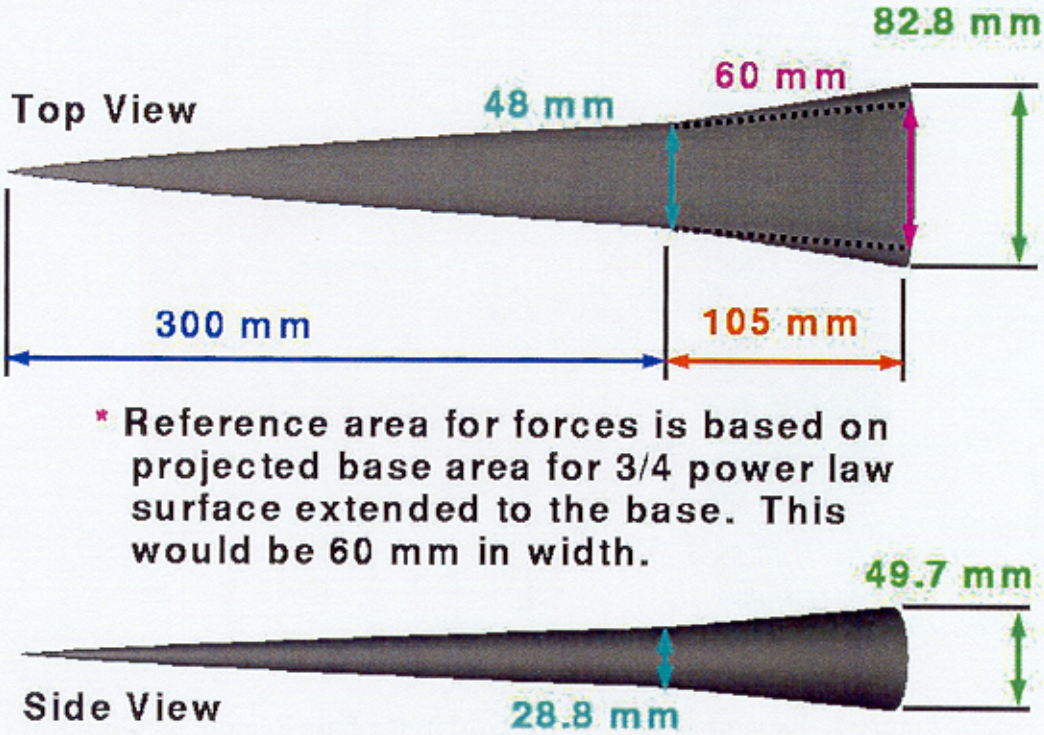

Figure 2. H3P78 Projectile.

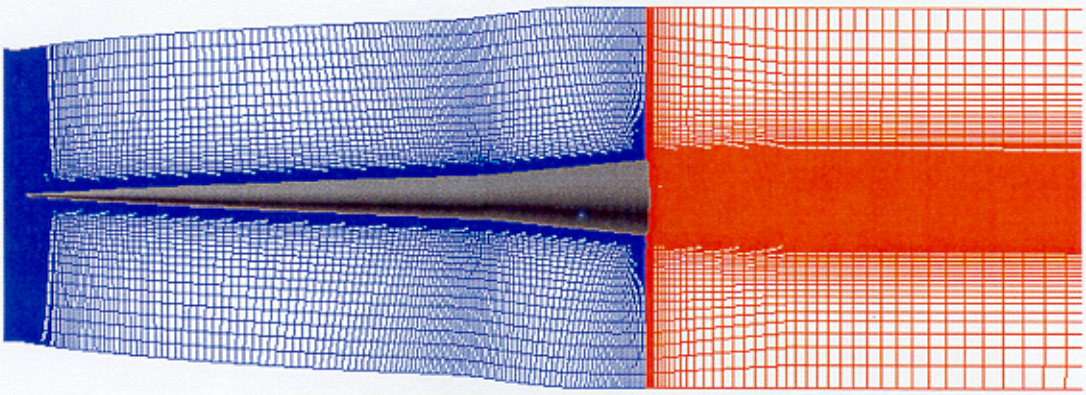

Figure 3. Full Grid for Viscous Computations, Jet Off.

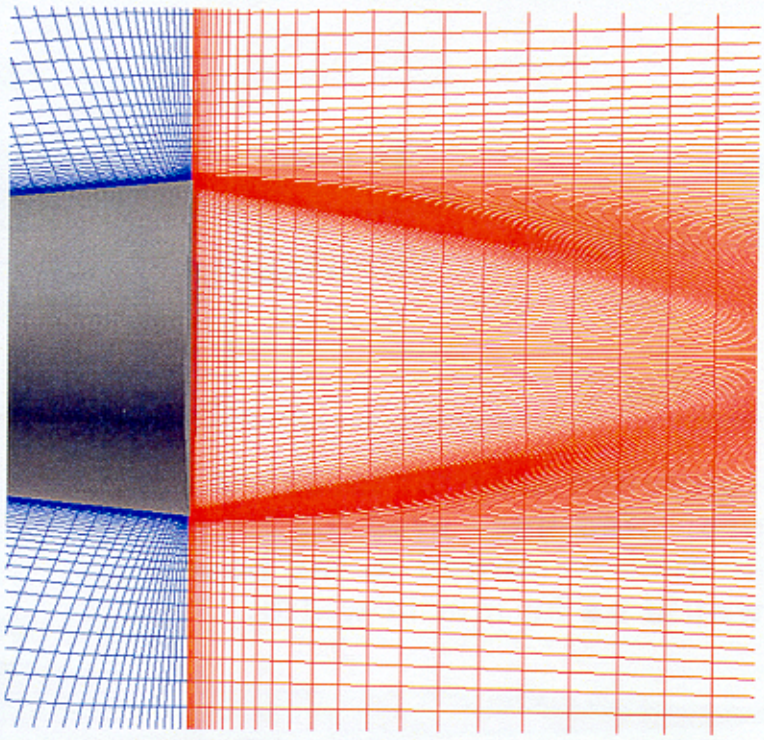

Figure 4. Expanded View of the Grid in the Base Region, Jet Off.

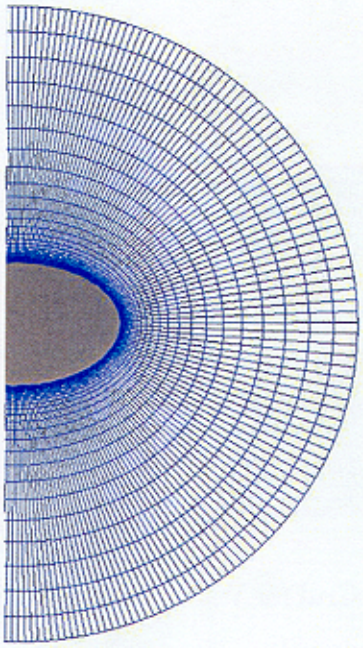

Figure 5. Circumferential Cross Section of the Grid at the Base.

For the jet-on cases, similar multi-block grids for the body were generated. The full grid for the jet-on case is shown in Figure 6, while an expanded view of the base region grid is shown in Figure 7. Here, for ease of grid generation, the chimera overset gridding technique (described earlier) was used to model the jet. The projectile body grid was generated first. The chimera technique allows the jet to be gridded separately. Two additional grid zones were created to model the jet. The dimensions for each zone are 21 x 20 x 40 and 10 x 10 x 40, in the longitudinal, circumferential, and normal directions. These two zones were then added to the projectile grid for the jet-on calculations, adding about 20,000 points to each grid. One of the jet grids is a cylindrical grid that covers the actual jet and extends beyond (see Figure 8). The second one is a rectangular grid placed within the actual jet and overset onto the other grid primarily to avoid the grid singularity along the centerline of the jet. An expanded view of the jet grids projected onto the projectile surface is shown in Figure 8. The jet grids and the body grids are all overset to form the complete mesh system. The chimera procedure results in hole boundaries (not shown here) in the body grid, which are attributable to the jet, and transfers information between the jet grids along these hole boundaries. The outer boundaries of the jet grids also receive information interpolated from the body mesh.

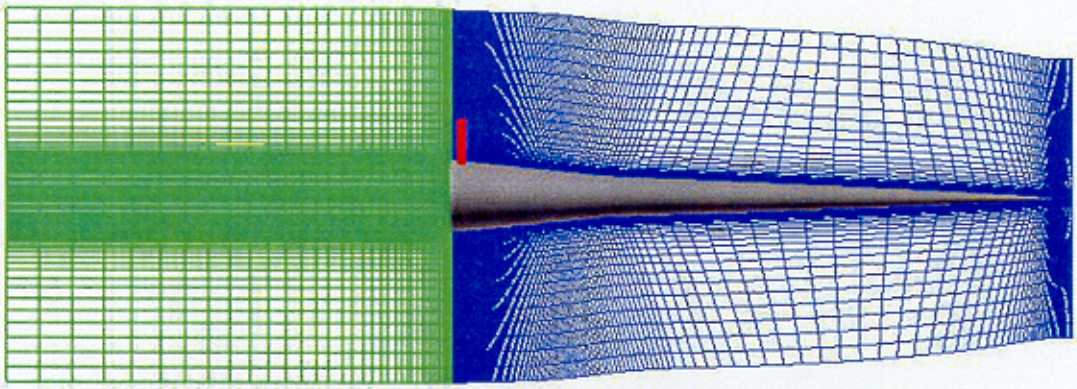

Figure 6. Full Grid for Viscous Computations, Jet On.

A fine mesh (GRID-3) was developed for the jet-on calculations (see Figure 6). With GRID-2 as a starting point, the number of longitudinal points was increased to 140, with the points more strategically placed along the projectile flare in the vicinity of the jet. The other grid zones were unchanged and were the same as previously described for GRID-2. The total number of points for GRID-3 is 1.3 million. Again, the minimum spacing at the wall is 2.0E-03 mm.

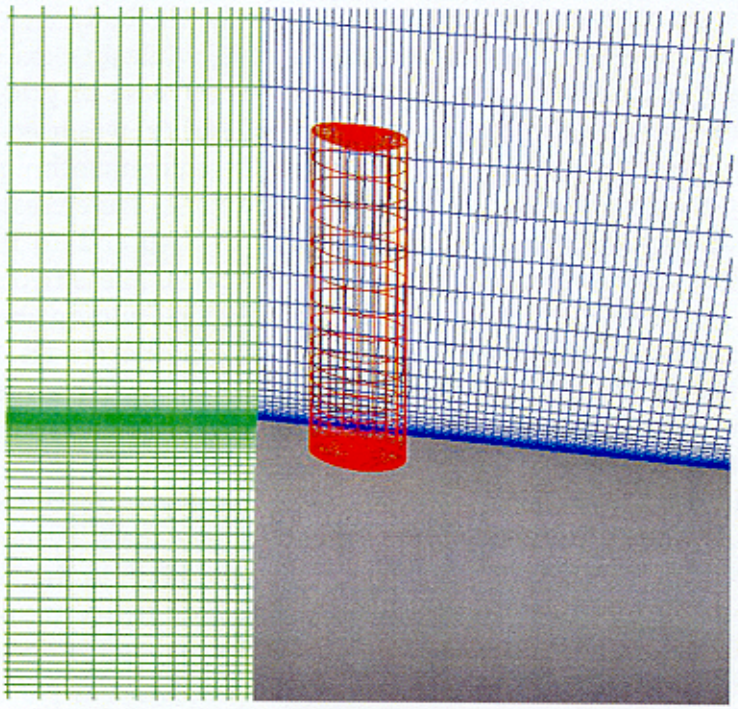

Figure 7. Expanded View of the Grid in the Base Region, Jet On.

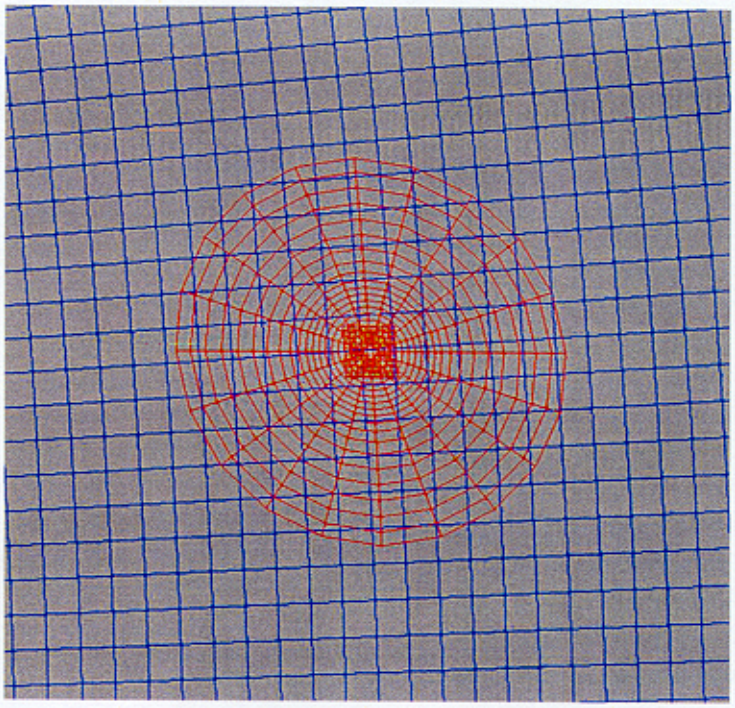

Figure 8. Expanded View of the Jet Grids Projected Onto the Projectile Surface.

5. Results

Steady state numerical computations using both Euler and viscous Navier-Stokes methods were performed to predict the flow field and aerodynamic coefficients on the H3P78 elliptical projectile for both jet-off and jet-on conditions. Three-dimensional calculations were performed at supersonic speeds between Mach 2.5 and 4.0 and several angles of attack between 0° and 12°. The projectile geometry and a set of experimental wind tunnel data for validation of the computations were supplied by DERA, UK, and DREV, Canada.

5.1 Zeus Euler Code Results (jet off)

Presented are results of computations for the H3P78 configuration. The Zeus GUI code was used to compute the flow field of the H3P78 at Mach numbers 2, 3, and 4. For each Mach number, the flow field was computed at multiple angles of attack. Figures 9, 10, and 11 show pressure contours of the H3P78 body and flow field at Mach 4. For the most part, Zeus captures the flow field features fairly well. However, Zeus was shown to be more accurate in predicting force and moments at lower angles of attack than at higher angles of attack for H-series projectiles. This may indicate that the lee side separation at higher angles of attack is producing flow field features that Zeus is not predicting accurately. Also note that Zeus can only perform the forebody flow field computation. Therefore, force and moments do not include the contribution of the base flow field.

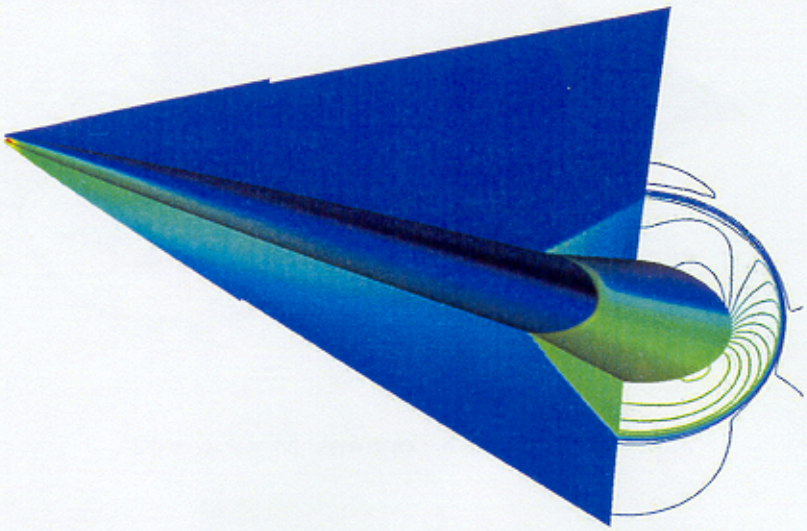

Figure 9. Pressure Contours, M = 4, $\alpha = 4°$.

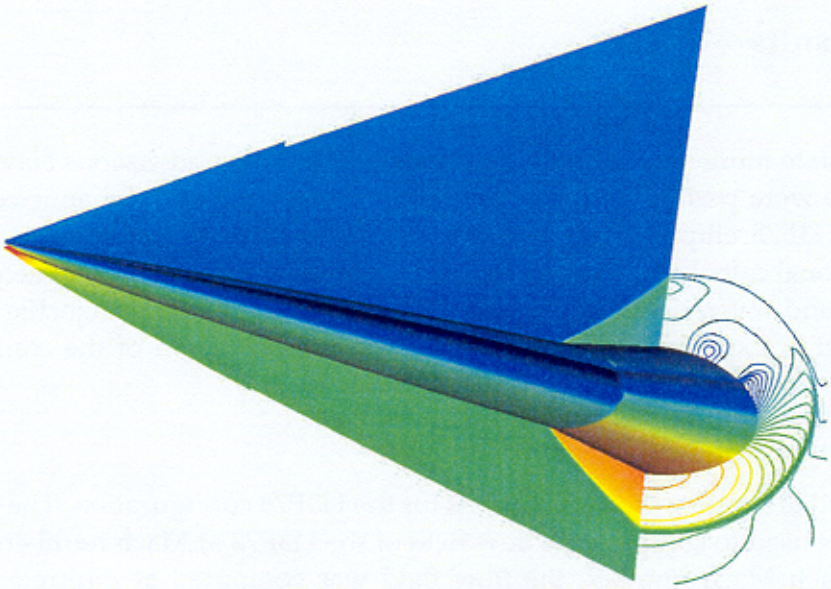

Figure 10. Pressure Contours, M = 4, $\alpha = 8°$.

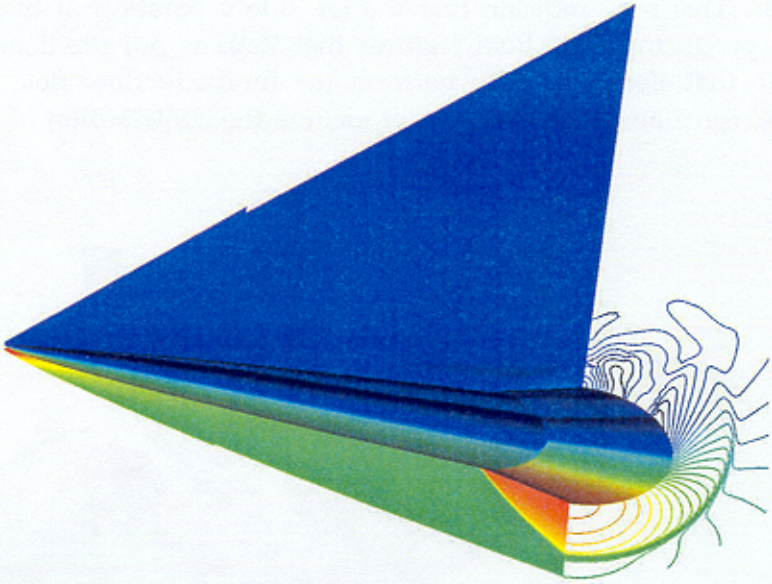

Figure 11. Pressure Contours, M = 4, $\alpha = 12°$.

Force and moments computed from the H3P78 flow fields are shown in Figures 12 through 15. In these cases, the moment coefficients were calculated about the nose of the projectile. Perhaps the most useful information that can be determined from a review of the plots is the information in Figure 15 that shows

how the forces are generated with body length. The plot indicates the extent to which the flare of the H3P78 contributes to the overall stability of the projectile. In general, the flare contributes greatly to the stability, but Figure 15 also indicates the substantial drag penalty attributable to the flare. This is indicated in Figure 15 by the increase in the slope of the axial force curve. In another study performed with a Zeus GUI, a comparison was made of stabilization by strakes and flare for a different H-series projectile [8]. The computations indicated that although the flare gave increased drag, it was still substantially more effective in providing stability than strakes alone. Overall, Zeus is a very good design tool for analyzing this type of trade-off.

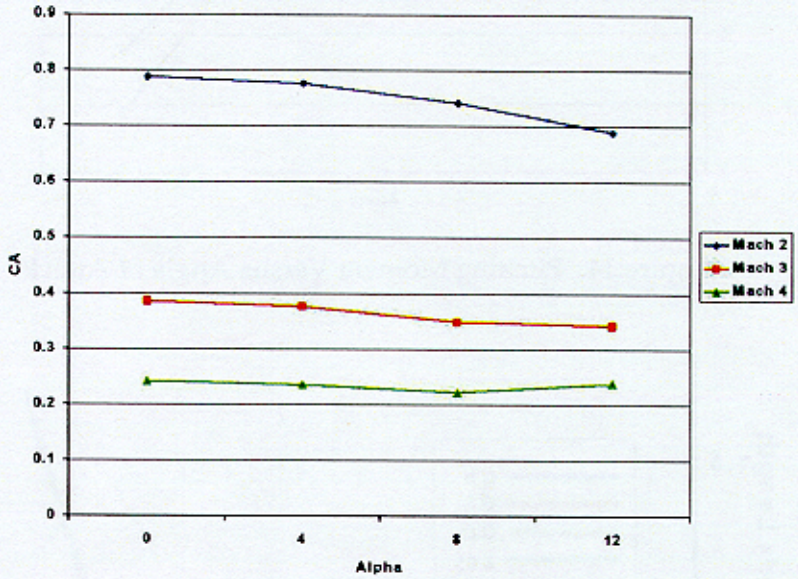

Figure 12. Axial Force Versus Angle of Attack.

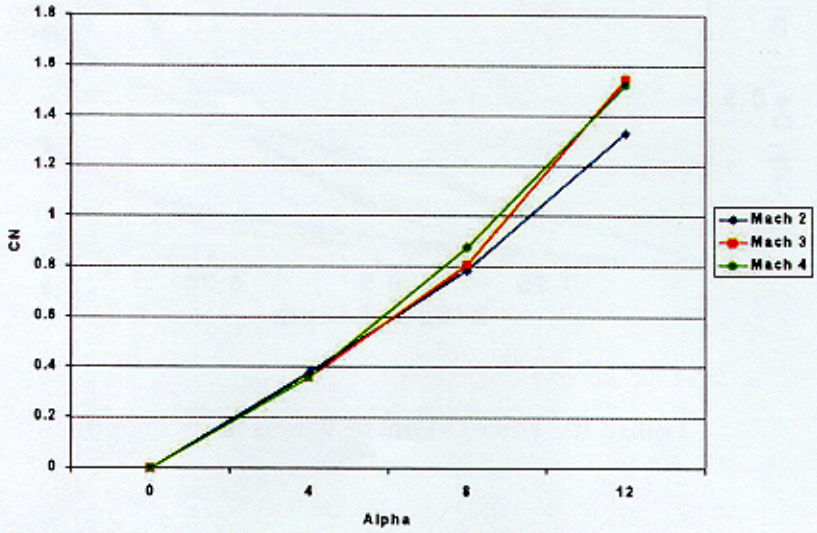

Figure 13. Normal Force Versus Angle of Attack.

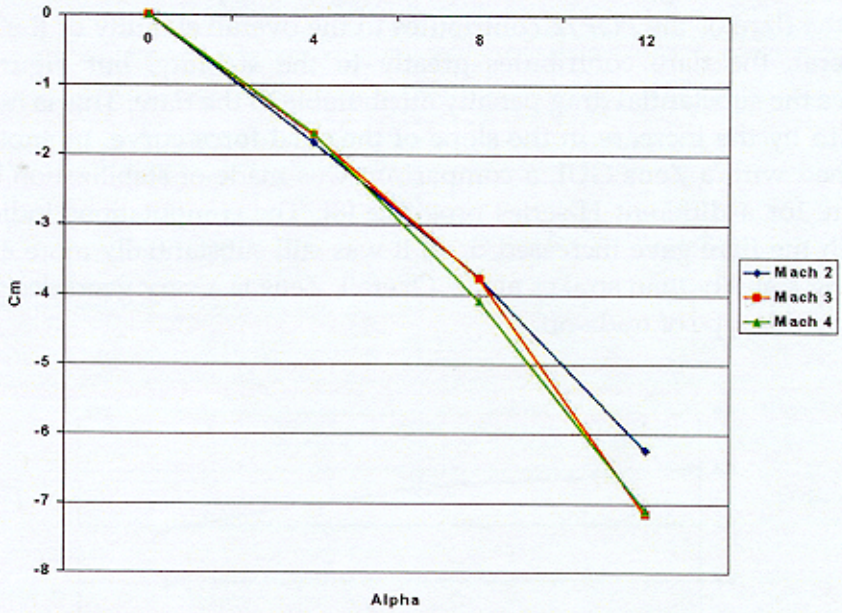

Figure 14. Pitching Moment Versus Angle of Attack.

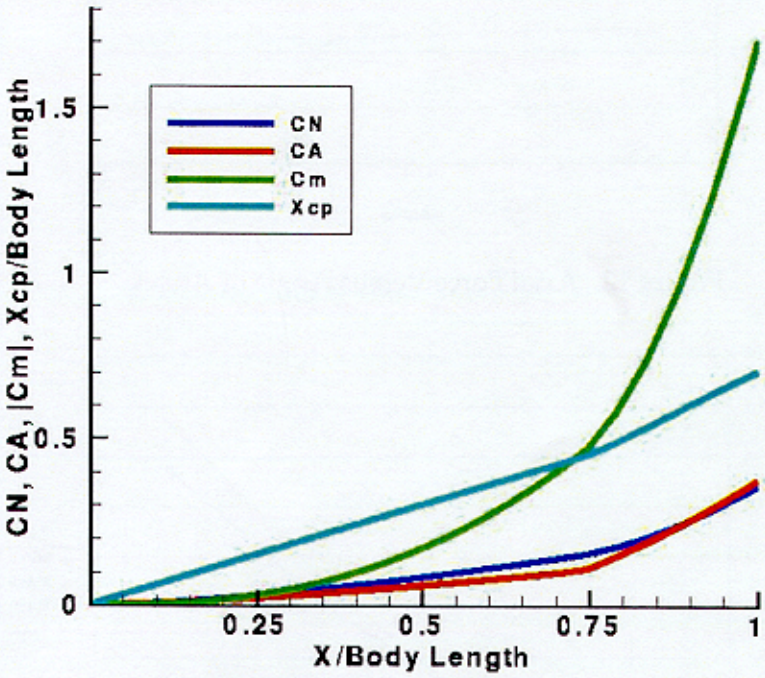

Figure 15. Force/Moment Versus Body Length.

5.2 Navier-Stokes Results (jet off)

Three-dimensional numerical computations have been performed for the H3P78 projectile with both ZNSFLOW and CFD++ codes at several supersonic Mach numbers between 2.5 and 4.0 and several angles of attack from 0° to 12° for the jet-off conditions. In addition, numerical computations for the H3P78 projectile have been performed for the jet-on conditions to study the interaction of a helium jet with a free stream M = 4.0 flow. All these simulations employ symmetry in the pitch plane, so only half of the physical domain is modeled. Turbulence closure was provided via either an algebraic model or a point-wise two-equation model. Computed results obtained for the jet-off conditions are presented next.

Figures 16 and 17, respectively, show computed pressure contours at M = 2.5 and 4.0 for different angles of attack. Here, blue represents low pressure and red represents high pressure regions. Figure 16 shows the computed pressure contours at Mach 2.5 and angles of attack 4, 8, and 12 degrees (from top to bottom). It shows the higher pressures on the wind side and lower pressures on the lee side. The lower pressures on the lee side can be seen more clearly, especially at 12 degrees angle of attack. Also seen in this figure are the shock waves emanating from the nose and the body-flare junction. Similar flow field features can be seen at Mach 4. As seen in Figure 17, the shock waves are stronger for M = 4 both at the nose and the flare junction. As the angle of attack increases from 4 to 12 degrees (from top to bottom), the computed pressure contours show an increase in the low pressure region on the lee side. Figure 18 shows the computed particle traces in the base region at M = 4.0 and α = 12 degrees. These particle traces show the complex vortical flow pattern in the near wake of the projectile.

Figures 19, 20, and 21 show the comparison of the computed aerodynamic force and moment coefficients with the data at M = 2.5. We obtained these computed force and moment coefficients by integrating the computed surface pressures. Figure 19 shows the comparison of the computed normal force coefficient with the data. The computed results shown here were obtained with both ZNSFLOW and CFD++ flow solvers. ZNSFLOW results were obtained with two different computational grids (grid 1 consisting of 1.8 million and grid 2 consisting of 1.0 million grid points) and show that the computed results are grid independent. The computed normal force obtained by both ZNSFLOW and CFD++ codes matches fairly well with the data except at 12 degrees angle of attack where a small discrepancy exists. The computed results with the ZNSFLOW code were obtained with an algebraic turbulence model, whereas the CFD++ results were obtained with a point-wise two-equation turbulence model. Figure 20 shows the comparison of the computed pitching moment coefficient with the experimental data. Again, the nose of the projectile is used as the reference point for the moment coefficient. In general, the computed pitching moment coefficient obtained by both Navier-Stokes solvers is in good agreement

with the data, regardless of the turbulence modeling used in the computations. The data and the computed results show that the pitching moment coefficient decreases as the angle of attack increases. A comparison of the computed axial force coefficient with the data is shown in Figure 21. The data and the computed results show that the drag is almost constant as a function of angle of attack. Again, the computed axial force coefficients are in good agreement and are within 10% of the measured data. The two different grids used in the ZNSFLOW computations produce almost identical results at higher angles of attack and are within 5% of each other at lower angles of attack. The computed results predicted by the CFD++ code seem to match the data slightly better except at 0 degree angle of attack.

Computations were performed for the H3P78 elliptical projectile at a higher Mach number, M = 4, and several angles of attack. Figures 22 through 25 show the comparison of the computed aerodynamic force and moment coefficients with the data at M = 4. Figure 22 shows the comparison of normal force coefficient at various angles of attack. The normal force increases with the increasing angles of attack, as seen in the computed and measured data. The computed data were obtained with Zeus Euler as well as the Navier-Stokes solvers and are shown in open symbols. The experimental data are shown in closed circles. All computed results are in excellent agreement with the data for all angles of attack. Computed results with the ZNSFLOW code again were obtained with an algebraic Baldwin-Lomax turbulence model, whereas the CFD++ results were obtained with a point-wise two-equation turbulence model. As seen in Figure 23, the computed pitching moment coefficients predicted by the Euler and Navier-Stokes techniques are in excellent agreement with experimental data. A comparison of the computed axial force coefficient with the data is shown in Figure 24. As expected, the largest discrepancy in the comparison is with the Euler code prediction. The Euler code underpredicts the axial force, as seen in Figure 24. The axial force coefficient predicted by the ZNSFLOW code matches well at 0 degree angle of attack and is within 10% of the measured data at other angles of attack. Computed results obtained with the CFD++ code are generally in very good agreement with the experimental data. The CFD++ code was also used to compute the flow fields at M = 4 for laminar flow conditions.

Figure 25 shows the comparison of laminar and turbulent runs with the data. The laminar results at all angles of attack are underpredicted, although the discrepancy seems to be less at higher angles of attack. The flow in the wake region behind the projectile (and thus the base drag) is predicted correctly in the turbulent runs, as evidenced by the very good comparison with the data.

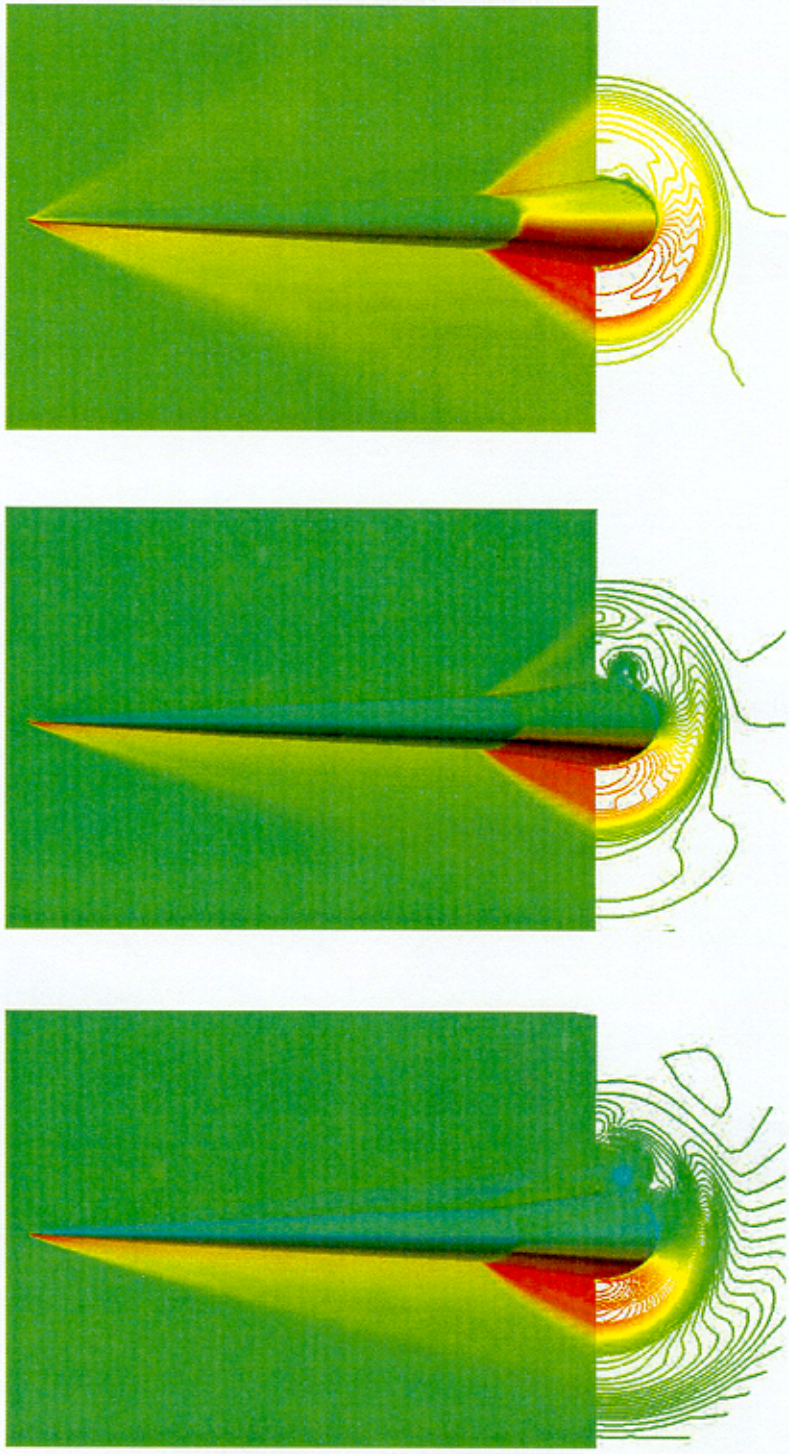

Figure 16. Computed Presure Contours, M = 2.5, α = 4°, 8°, 12° (top to bottom).

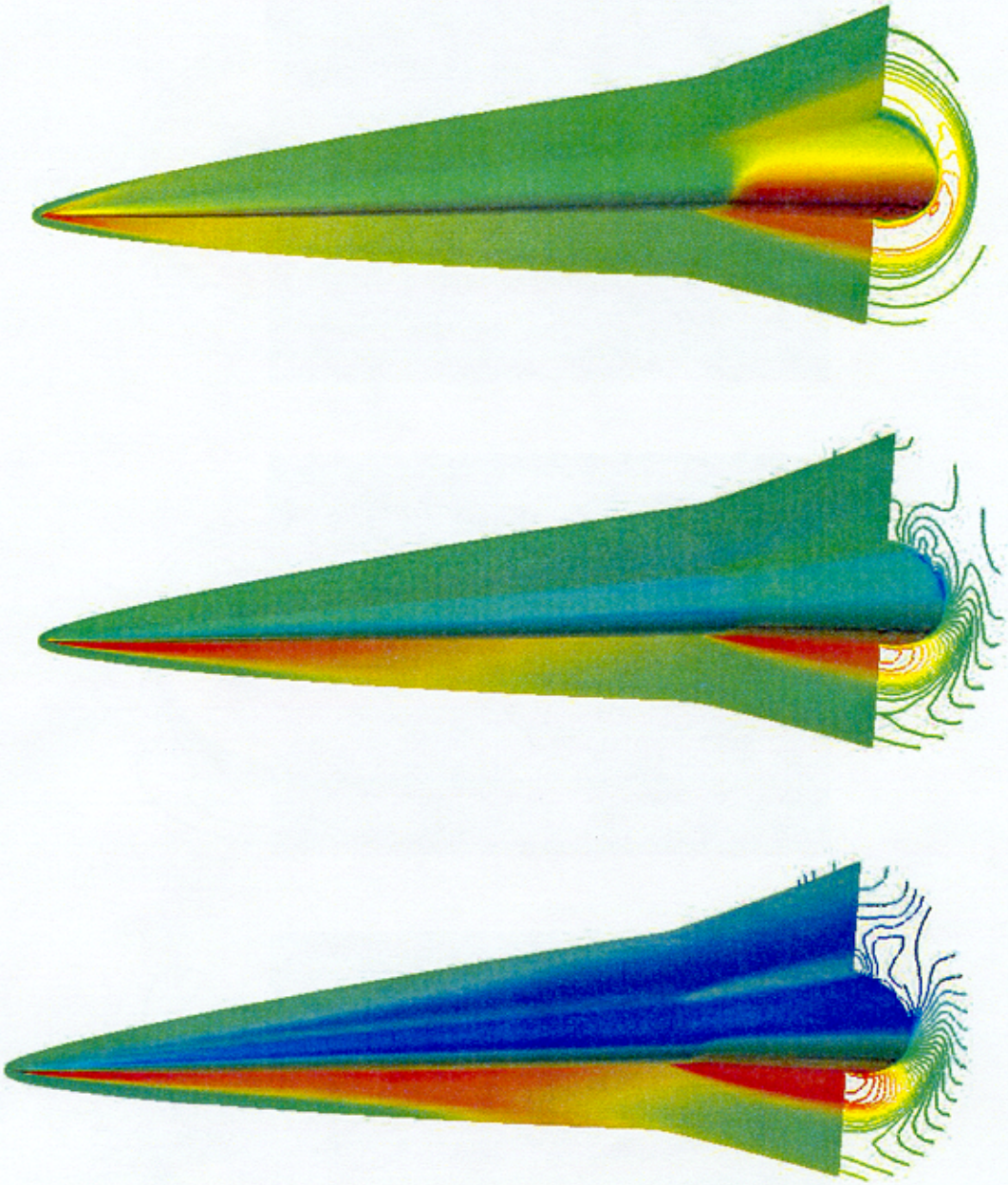

Figure 17. Computed Pressure Contours, M= 4.0, α = 4°, 8°, 12° (top to bottom).

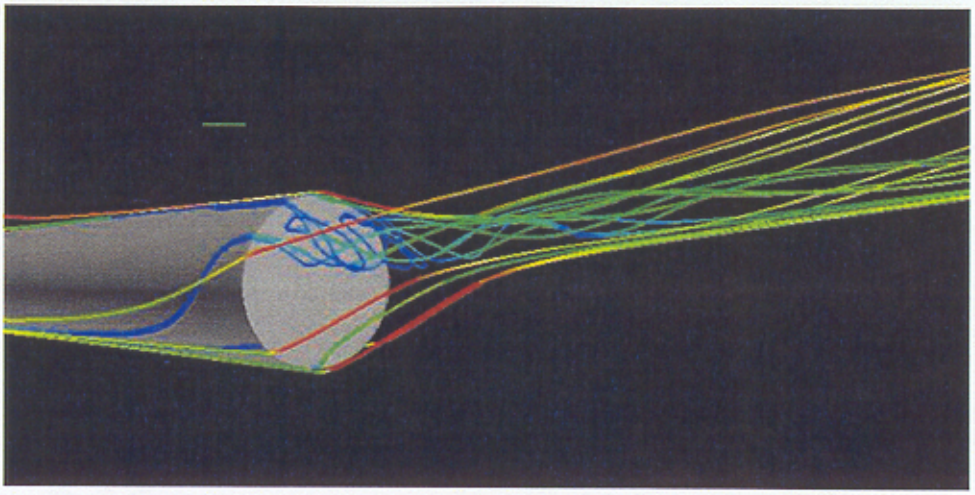

Figure 18. Computed Particle Traces, M = 4.0, α = 12.

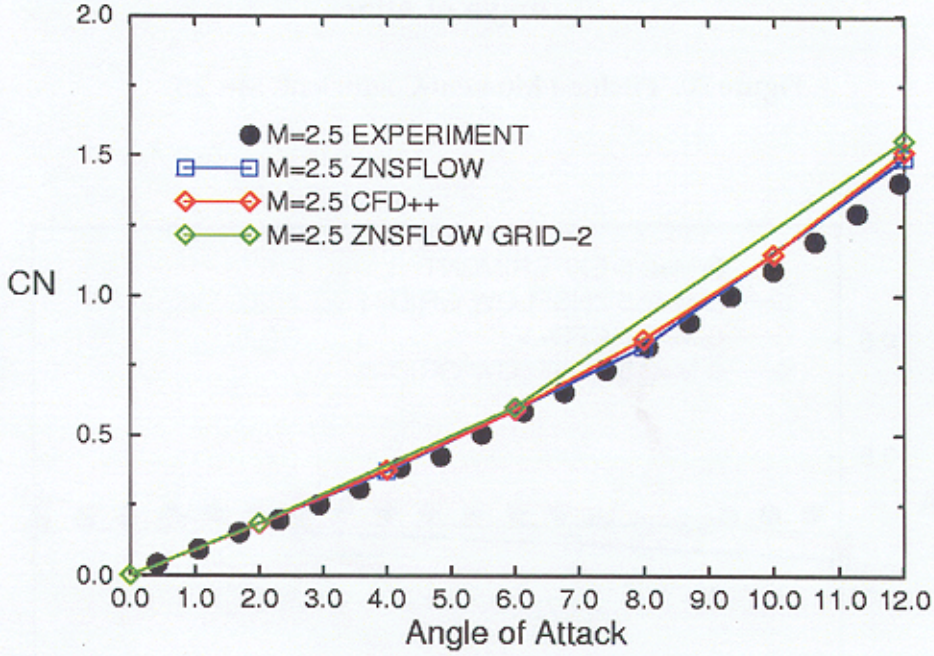

Figure 19. Normal Force Coefficient, M = 2.5.

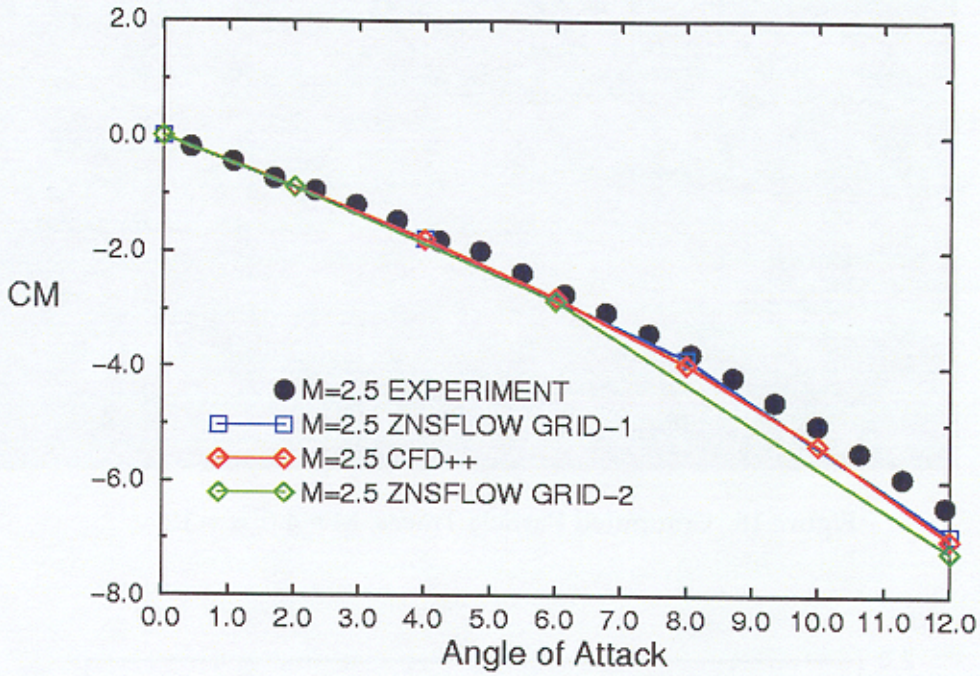

Figure 20. Pitching Moment Coefficient, M= 2.5.

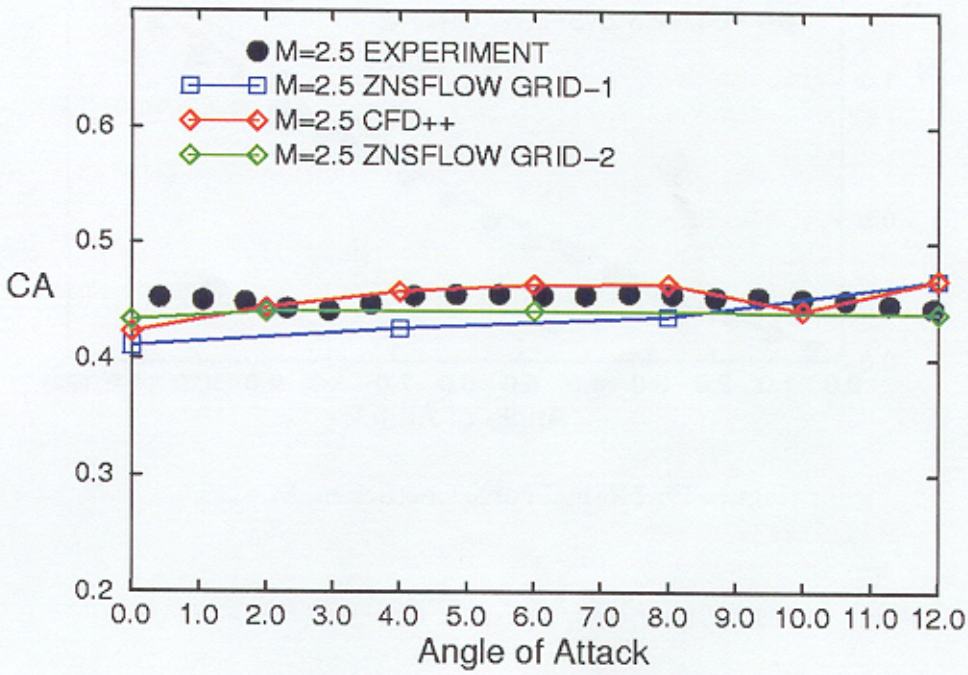

Figure 21. Axial Force Coefficient, M = 2.5.

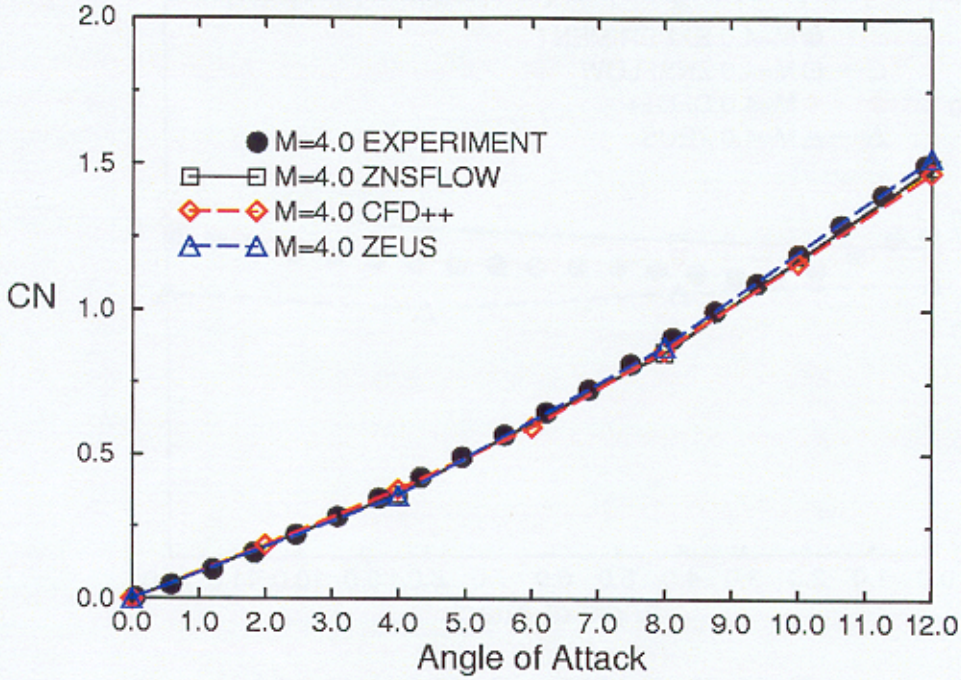

Figure 22. Normal Force Coefficient, M = 4.0.

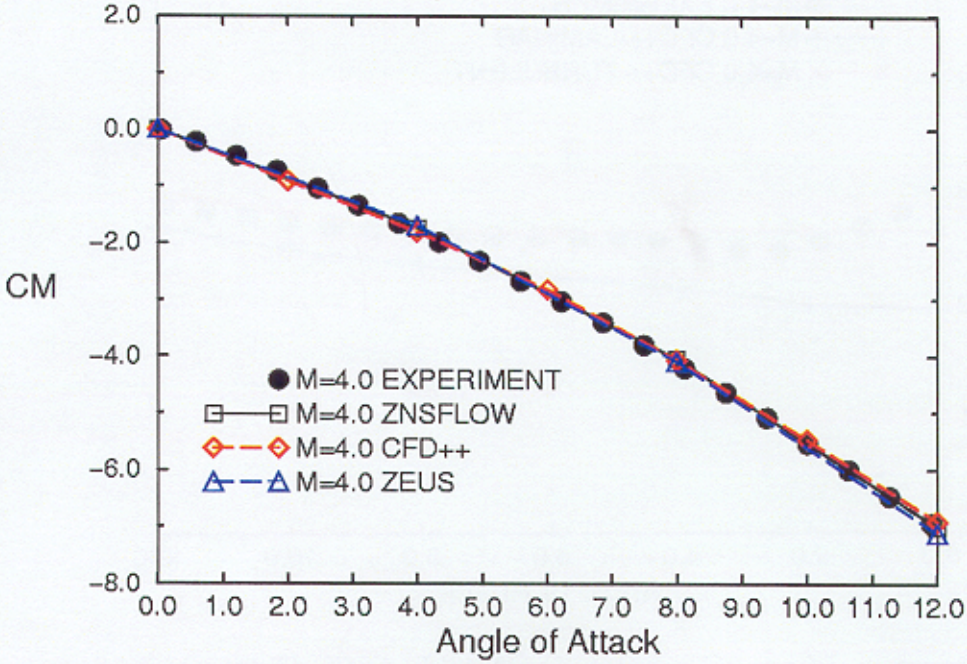

Figure 23. Pitching Moment Coefficient, M = 4.0.

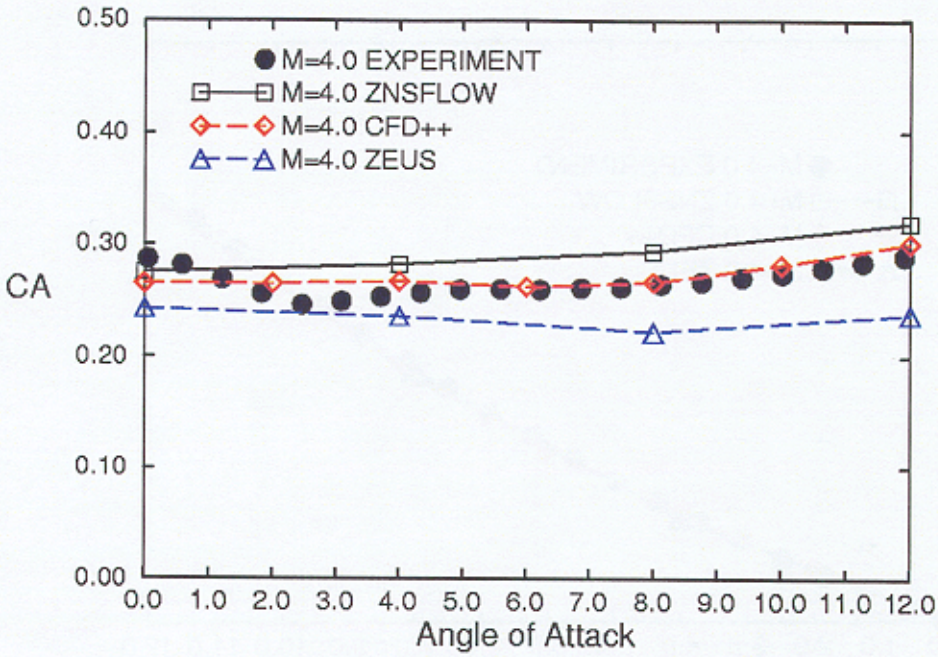

Figure 24. Axial Force Coefficient, M = 4.0.

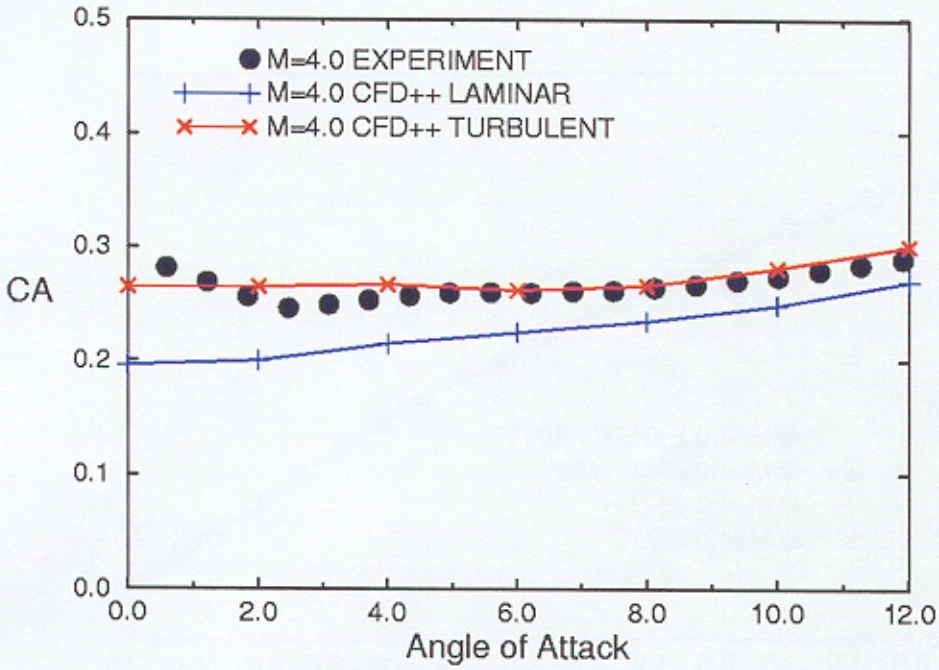

Figure 25. Effects of Turbulence on Axial Force Coefficient, M = 4.0.

5.3 Jet-On Results

Three-dimensional calculations at Mach 4.0 and several angles of attack between 0° and 12° were performed for the same elliptical projectile (see Figure 26) for the jet-on conditions. These numerical computations were performed for the jet-on conditions to study the interaction of a helium jet with a free stream M = 4.0 flow.

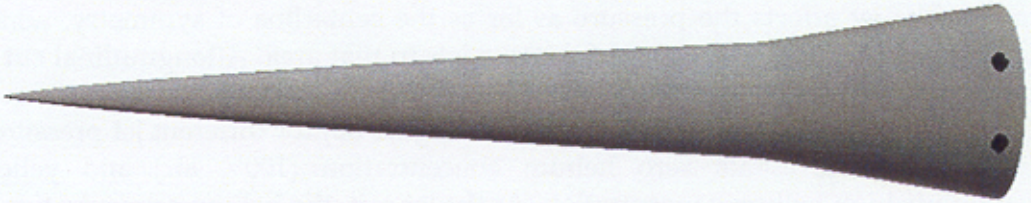

Figure 26. H3P78 Projectile, Showing the Jet Locations.

The real gas version of the CFD++ code was used. A point-wise two-equation turbulence model was used and integrated all the way to the wall. Because of symmetry, only one of the two jets has been modeled in the computations. The ratio of the jet to free stream pressure was varied from 156 (100% jet pressure) to 39 (25% jet pressure). The velocity of the jet was set at 872 meters per second. Again, the projectile geometry and a set of experimental wind tunnel data for validation of the computations were supplied by DERA, UK **[23]**.

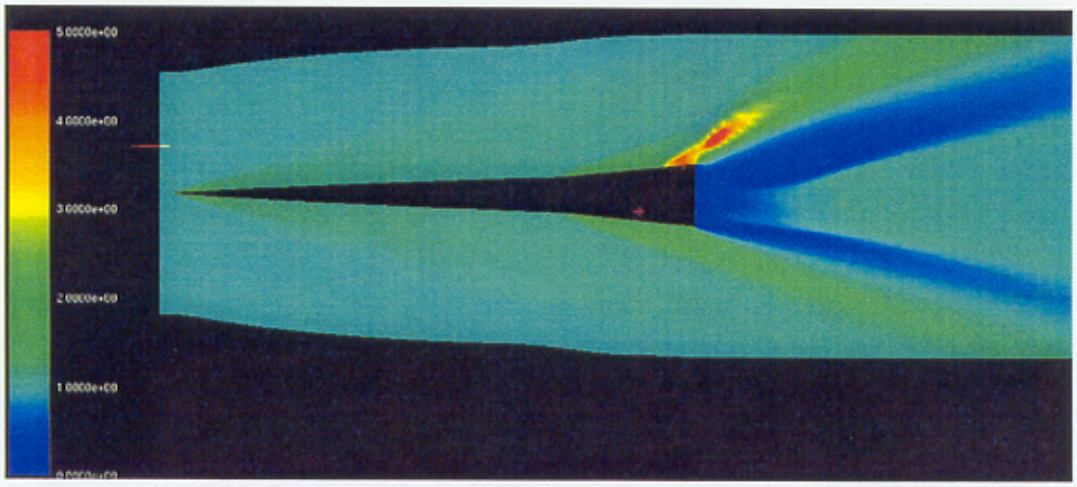

Figure 27. Computed Pressure Contours, Jet On, 100% Jet Pressure, M = 4.0, α = 0°.

The computed pressure contours in the symmetry plane are shown in Figure 27. Here, the low pressure region is indicated in blue and high pressures are indicated in red. The red region on the lee side shows the effect of the jet upstream and on the incoming free stream flow. As expected, the pressure in the

base region or in the near wake is low. The flow upstream from the flare junction remains unaltered. An expanded view of the pressure contours in the base region and in the vicinity of the jet is shown in Figure 28. It clearly shows the effect of the jet on the lee side flow field. The pressure field on the wind side looks similar to that of the jet-off case. A circumferential view of the surface pressures on the projectile after-body is shown in Figure 29. It clearly shows the strong effect of the jet in all directions for the 50% jet pressure case. The surface pressure in front of the jet is increased while the surface pressure downstream from the jet is lower. The jet affects the pressure as far as the centerline of symmetry, which indicates the strong interaction of the two jets in that area. A longitudinal cut at the jet centerline was selected and used to show the concentration of helium in that plane containing the jet centerline (see Figure 30) for different jet pressures. Here, black represents zero helium concentration (100% air) and yellow represents high helium concentration. At the jet exit, the helium concentration is one. This figure clearly shows the helium jet interacting with the free stream computed surface pressure contours for the three different jet pressure cases. Computed surface pressures have been obtained along the centerline of symmetry as well as along the centerline of the jet itself. These surface pressures are used to study the effect of the aerodynamic interference resulting from the jet interaction with the free stream flow. Computed surface pressures have been compared with the experimental data. Figure 31 shows the comparison of the computed surface pressures with the data measured along the centerline of symmetry for various jet pressure cases. The computed results here are shown as symbols and the data are shown as lines.

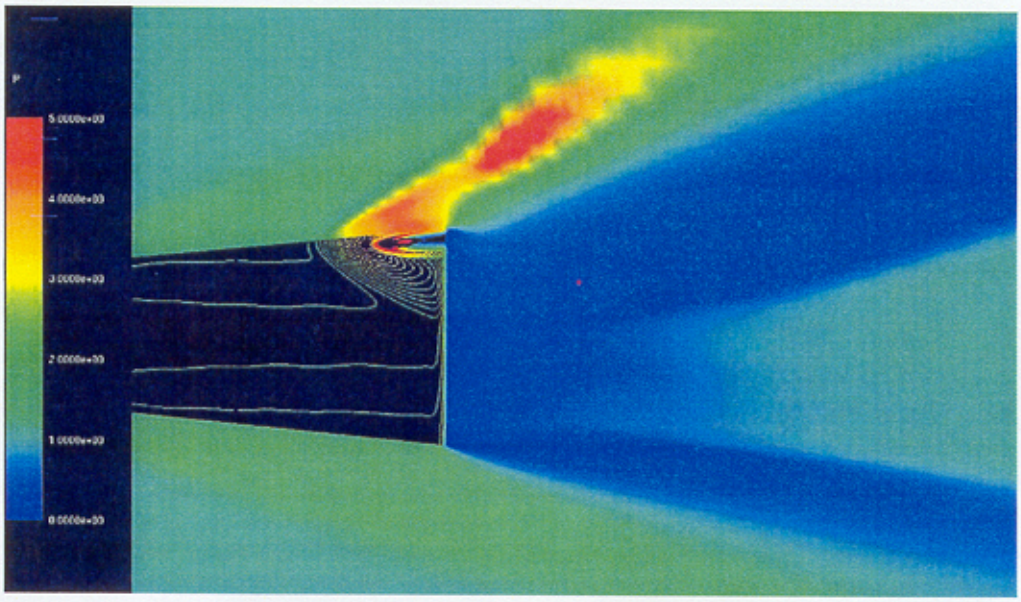

Figure 28. Computed Pressure Contours Near the Jet and Wake, Jet On, 100% Jet Pressure, M = 4.0, $\alpha = 0°$.

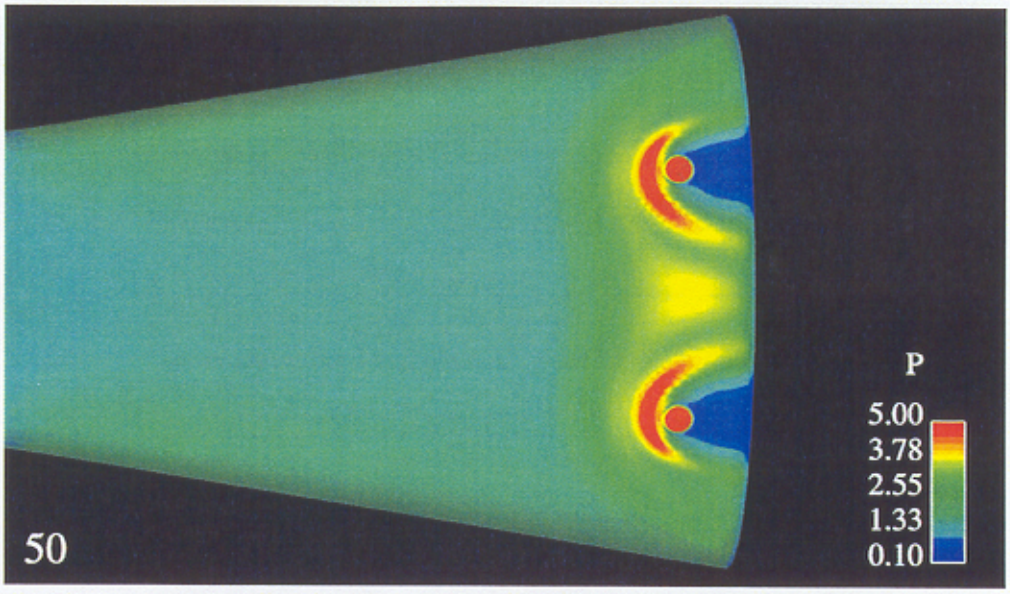

Figure 29. Computed Surface Pressure Contours Near the Jet, 50% Jet Pressure, $M = 4.0$, $\alpha = 0°$.

CFD and the data show a pressure rise; however, the numerical predictions indicate a much stronger jet-to-jet interaction than is indicated by the data. The pressure rise is somewhat decreased with decreasing jet pressures. The computed results presented here used the fine mesh (grid 3), and it is believed that the discrepancy is not attributable to the number of mesh points used in the computations.

The comparison of the computed surface pressures along the centerline of the jet for various jet pressure cases is shown in Figure 32. Again, computed results have been compared with the available data. Except for the 100% jet pressure case, the computed results are in good agreement with the measured data. CFD and the data clearly show the expected pressure rise ahead of the jet. Also, this figure shows the lower pressures downstream from the jet (pressure less than the free stream static pressure). Although not shown here, this level of lower pressure downstream from the jet is also very similar to that measured in the experiment. All the flow field effects associated the jet interaction have not yet fully been analyzed. Overall, the computed flow field around the projectile and the jet showed similar characteristics as those observed in the experiment.

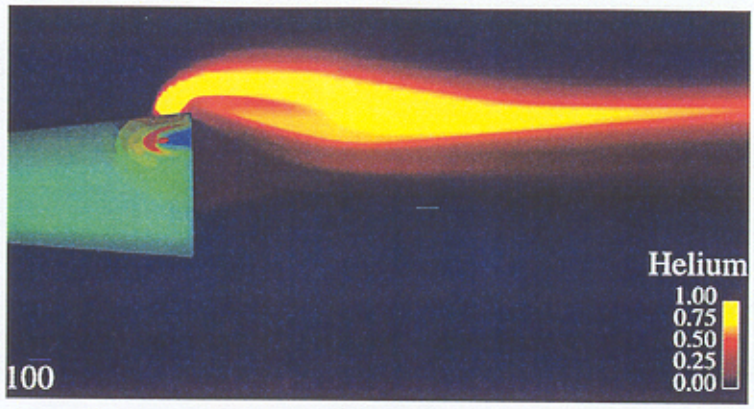

(a)

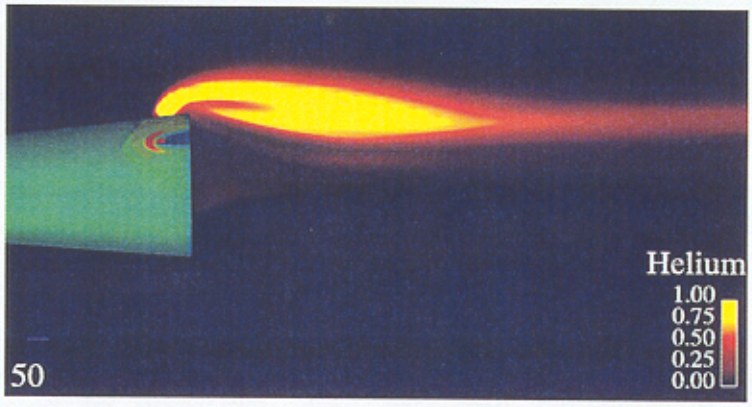

(b)

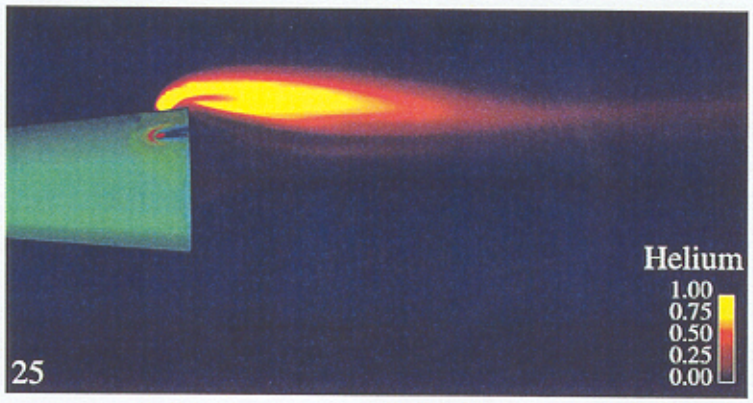

(c)

Figure 30. Computed Helium Concentration Contours Near the Base Region, (a) 100%, (b) 50%, and (c) 25% Jet Pressures, M = 4.0, $\alpha = 0°$.

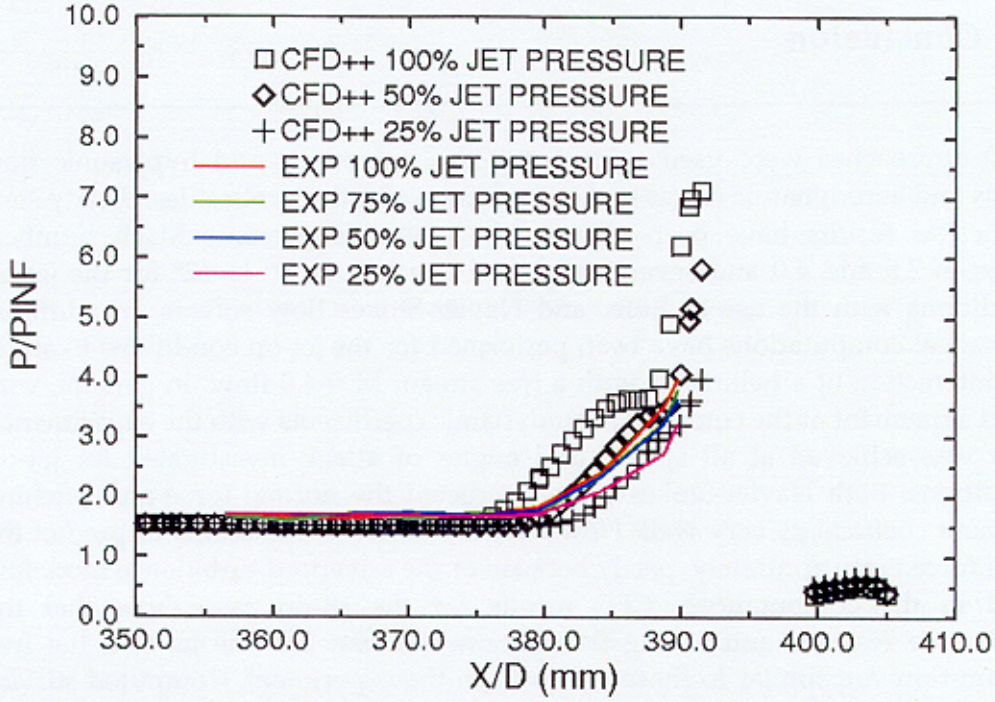

Figure 31. Surface Pressure Contours Comparison Along the Centerline of Symmetry, M = 4.0, $\alpha = 0°$.

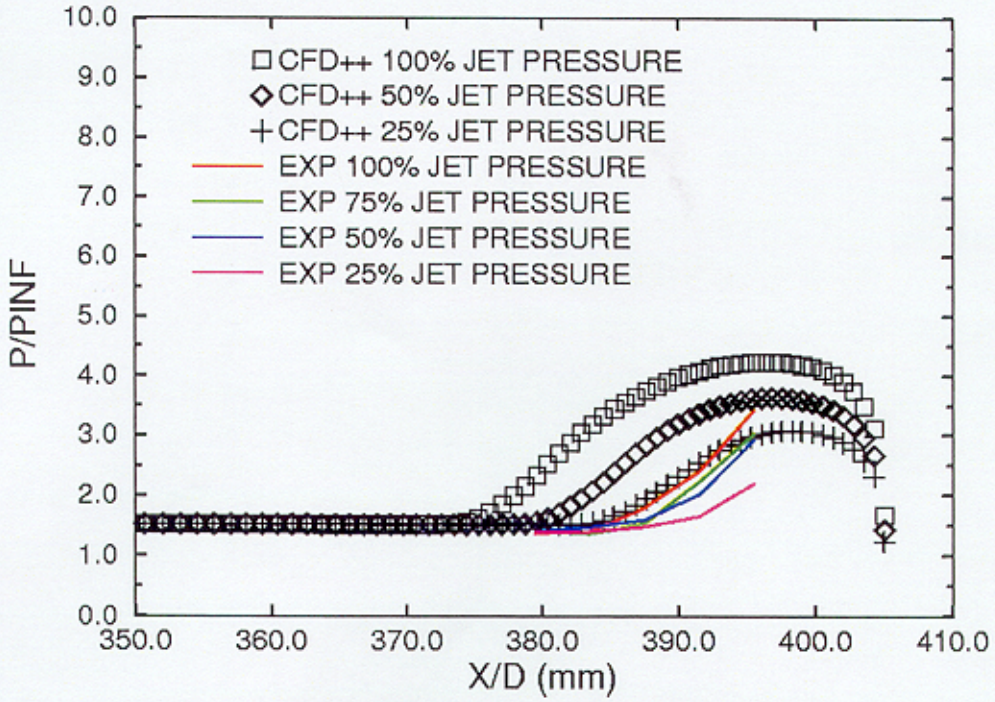

Figure 32. Surface Pressure Contours Comparison Along the Centerline of Jet, M = 4.0, $\alpha = 0°$.

6. Conclusion

CFD approaches were used to compute the supersonic and hypersonic flow fields and aerodynamic forces and moments on elliptical projectiles. Steady state numerical results have been obtained at several supersonic Mach numbers between 2.5 and 4.0 and several angles of attack from 0° to 12° for the jet-off conditions with the use of Euler and Navier-Stokes flow solvers. In addition, numerical computations have been performed for the jet-on conditions to study the interaction of a helium jet with a free stream M = 4.0 flow. In general, very good agreement of the computed aerodynamic coefficients with the experimental data was achieved at all speeds and angles of attack investigated for jet-off conditions. Both Navier-Stokes codes predicted the normal force and pitching moment coefficients very well. However, the CFD++ code seems to predict the axial force more accurately, partly because of the advanced turbulence modeling used in the computations. CFD results for the jet-on case show that the qualitative features and strong flow interaction between the jet and the free stream flow are similar to those observed in the experiment. Computed surface pressures along the jet centerline compare better than those along the line of symmetry. The results show the predictive capabilities of CFD techniques for supersonic flow over elliptical projectiles with and without jet interaction.

References

1. Sahu, J., K.R. Heavey, and E.N. Ferry, "Computational Fluid Dynamics for Multiple Projectile Configurations," Proceedings of the 3rd Overset Composite Grid and Solution Technology Symposium, Los Alamos, NM, October 1996.

2. Sahu, J., K.R. Heavey, and C.J. Nietubicz, "Time-Dependent Navier-Stokes Computations for Submunitions in Relative Motion," Proceedings of the 6th International Symposium on Computational Fluid Dynamics, Vol. III, pp. 1020-1027, Lake Tahoe, NV, September 1995.

3. Sahu, J., K.R. Heavey, and C.J. Nietubicz, "Computational Modeling of SADARM Submunition Separation," Journal of Computer Modeling and Simulation in Engineering, Vol. 2, pp. 267-283, July 1997.

4. Sahu, J., K.R. Heavey, and E.N. Ferry, "Computational Modeling of Multibody Aerodynamic Interference," Journal of Advances in Engineering Software, Vol. 29, No. 3-6, pp. 383-388, Elsevier Sciences, Apr-Jul 1998.

5. Orchard, D., E. Fournier, A. Dupuis, and J. Edwards, "Wind Tunnel Tests on the H3P78, Power Law, Elliptic Section Flared Projectile from Mach 2.5 to 4," AIAA Paper No. 2001-4321, American Institute of Aeronautics and Astronautics, Montreal, Canada, August 2001.

6. Edge, H.L., and J. Clarke, "Graphical User Interface for Zeus," ARL-TR-1443, U.S. Army Research Laboratory, Aberdeen Proving Ground, MD, June 1996.

7. Edge, H.L., and J. Clarke, "Computation of Noncircular and Circular Missile Flow Fields With Graphical User Interface Driven Zeus," in Military, Government and Aerospace Simulation, Simulation Series Vol. 29, No. 4, Atlanta, GA, April 1997.

8. Boyle, C., "Inviscid Aerodynamic Predictions of Hypersonic Elliptical Projectiles: A Comparative Study of the Effects of Stabilizing Surfaces," Naval Postgraduate School, Monterey, CA, June 2000.

9. Edge, H.L., J. Sahu, K.R. Heavey, et al., "Common High Performance Computing Software Support Initiative (CHSSI) Computational Fluid Dynamics (CFD)-6 Project Final Report: ARL Block-Structured Gridding Zonal Navier-Stokes (ZNSFLOW) Solver Software," ARL-TR-2084, U.S. Army Research Laboratory, Aberdeen Proving Ground, MD, February 2000.

10. Peroomian, O., S. Chakravarthy, and U. Goldberg, "A 'Grid-Transparent' Methodology for CFD," AIAA Paper 97-0724, 35th Aerospace Sciences Meeting, Reno, NV, January 1997.

11. Peroomian, O., S. Chakravarthy, S. Palaniswamy, and U. Goldberg, "Convergence Acceleration for Unified Grid Formulation Using Preconditioned Implicit Relaxation," AIAA Paper 98-0116, 36th Aerospace Sciences Meeting, Reno, NV, January 1998.

12. Fournier, E., and D. Orchard, "Testing of a Novel Maneuvering Projectile in the DREV Trisonic Wind Tunnel," Technical Memorandum Report, DREV TM-2000-108, Defence Research Establishment, Valcartier, Canada, July 2000.

13. Wardlaw, A., and S. Davis, "A Second Order Godunov Method for Supersonic Tactical Missiles," NSWC TR 86-506, Naval Surface Weapons Center, Silver Spring, MD, December 1986.

14. Wardlaw, A., and F. Priolo, "Applying the ZEUS Code," NSWC TR 86-508, Naval Surface Weapons Center, Silver Spring, MD, December 1986.

15. Sahu, J., K.R. Heavey, D.M. Pressel, and S. Dinavahi, "Parallel Numerical Computations of Projectile Flow Fields," AIAA 17th Applied Aerodynamics Conference, Norfolk, VA, June 1999.

16. Steger, J.L., S.X. Ying, and L.B. Schiff, "A Partially Flux-Split Algorithm for Numerical Simulation of Compressible Inviscid and Viscous Flows," Proceedings of the Workshop on CFD, Institute of Nonlinear Sciences, University of California, Davis, CA, 1986.

17. Steger, J.L., F.C. Dougherty, and J.A. Benek, "A Chimera Grid Scheme," Advances in Grid Generation, edited by K. N. Ghia and U. Ghia, ASME FED-5, June 1983.

18. Benek, J.A., T.L. Donegan, and N.E. Suhs, "Extended Chimera Grid Embedding Scheme With Application to Viscous Flows," AIAA Paper No. 87-1126-CP, 8th AIAA Computational Fluid Dynamics Conference, Honolulu, HI, June 1987.

19. Meakin, R., and A. Wissink, "Unsteady Aerodynamic Simulation of Static and Moving Bodies Using Scalable Computers," AIAA-99-3302-CP, 14th AIAA Computational Fluid Dynamics Conference, Norfolk, VA, June 1999.

20. Baldwin, B.L., and H. Lomax, "Thin Layer Approximation and Algebraic model for Separated Turbulent Flows," AIAA 78-257, American Institute of Aeronautics and Astronautics, Montreal, Canada, January 1978.

21. Goldberg, U.C., O. Peroomian, and S. Chakravarthy, "A Wall-Distance-Free K-E Model With Enhanced Near-Wall Treatment," American Society of Mechanical Engineers, Journal of Fluids Engineering, Vol. 120, pp. 457-462, 1998.

22. Pulliam, T.H., and J.L. Steger, "On Implicit Finite-Difference Simulations of Three-Dimensional Flow," AIAA Journal, Vol. 18, No. 2, pp. 159-167, February 1982.

23. Orchard, D., E. Fournier, A. Dupuis, and J. Edwards, "Wind Tunnel Tests on the H3P78, Power Law, Elliptic Section Flared Projectile with Jet Interaction," AIAA Paper No. 2001-4322, Montreal, Canada, August 2001.

INTENTIONALLY LEFT BLANK

NO. OF COPIES	ORGANIZATION
1	ADMINISTRATOR DEFENSE TECHNICAL INFO CTR ATTN DTIC OCA 8725 JOHN J KINGMAN RD STE 0944 FT BELVOIR VA 22060-6218
1	DIRECTOR US ARMY RSCH LABORATORY ATTN AMSRL CI AI R REC MGMT 2800 POWDER MILL RD ADELPHI MD 20783-1197
1	DIRECTOR US ARMY RSCH LABORATORY ATTN AMSRL CI LL TECH LIB 2800 POWDER MILL RD ADELPHI MD 20783-1197
1	DIRECTOR US ARMY RSCH LABORATORY ATTN AMSRL D D SMITH 2800 POWDER MILL RD ADELPHI MD 20783-1197
2	USAF WRIGHT AERONATCL LABS ATTN AFWAL FIMG DR J SHANG MR N E SCAGGS WRIGHT PATTERSON AFB OH 45433-6553
2	CDR NAVAL SURF WARFARE CTR ATTN CODE B40 DR W YANTA DR F MOORE DAHLGREN VA 22448-5100
1	CDR NAVAL SURF WARFARE CTR ATTN CODE 420 DR A WARDLAW INDIAN HEAD MD 20640-5035
4	DIRECTOR NASA LANGLEY RSCH CTR ATTN TECH LIBRARY MR D M BUSHNELL DR M J HEMSCH DR J SOUTH LANGLEY STATION HAMPTON VA 23665
1	LOS ALAMOS NATL LAB ATTN MS G770 BILL HOGAN LOS ALAMOS NM 87545

NO. OF COPIES	ORGANIZATION
2	DARPA ATTN DR P KEMMEY DR J RICHARDSON 3701 NORTH FAIRFAX DR ARLINGTON VA 22203-1714
5	DIRECTOR NASA AMES RSCH CTR ATTN MS 227 8 L SCHIFF MS 258 1 T HOLST MS 258 1 D CHAUSSEE MS 258 1 M RAI MS 258 1 B MEAKIN MOFFETT FIELD CA 94035
4	CDR US ARMY TACOM ARDEC ATTN AMSTA AR FSF T C NG H HUDGINS J GRAU W KOENIG BLDG 382 PICATINNY ARSENAL NJ 07806-5000
1	CDR US ARMY TACOM-ARDEC ATTN AMCPM DS MO P BURKE BLDG 162S PICATINNY ARSENAL NJ 07806-5000
1	CDR US ARMY TACOM ATTN AMSTA-AR-CCH-B P VALENTI BLDG 65-S PICATINNY ARSENAL NJ 07806-5001
1	CDR US ARMY ARDEC ATTN SFAE FAS SD MIKE DEVINE PICATINNY ARSENAL NJ 07806-5001
2	UNIV OF CALIFORNIA DAVIS DEPT OF MECHANICAL ENGG ATTN PROF H A DWYER PROF M HAFEZ DAVIS CA 95616
1	AEROJET ELECTRONICS PLANT ATTN B170 DEPT 5311 D PILLASCH PO BOX 296 1100 W HOLLYVALE ST AZUSA CA 91702

NO. OF COPIES	ORGANIZATION
3	AIR FORCE ARMAMENT LAB ATTN AFATL/FXA S C KORN B SIMPSON D BELK EGLIN AFB FL 32542-5434
1	MASS INST OF TECHNOLOGY ATTN TECH LIBRARY 77 MASSACHUSETTS AVE CAMBRIDGE MA 02139
3	DIR SANDIA NATL LABS ATTN DIV 1554 DR W OBERKAMPF DIV 1554 DR F BLOTTNER DIV 1636 DR W WOLFE ALBUQUERQUE NM 87185
1	NAVAL AIR WARFARE CTR ATTN MS 3 DAVID FINDLAY BLDG 2187 PATUXENT RIVER MD 20670
1	METACOMP TECHNOLOGIES INC ATTN S R CHAKRAVARTHY 650 HAMPSHIRE RD STE 200 WESTLAKE VILLAGE CA 91361-2510
4	CDR USAAMCOM ATTN AMSAM RD SS G LANDINGHAM AMSAM RD SS AS E KREEGER C MIKKELSON E VAUGHN REDSTONE ARSENAL AL 35898-5252
1	ADVANCED TECHNOLOGY CTR ARVIN/CALSPAN AERODYNAMICS RSCH DEPT ATTN DR M S HOLDEN PO BOX 400 BUFFALO NY 14225
1	UNIV OF ILLINOIS AT URBANA CHAMPAIGN DEPT OF MECH & INDUS ENGNG ATTN DR J C DUTTON URBANA IL 61801
1	UNIV OF MARYLAND DEPT OF AEROSPACE ENGG ATTN DR J D ANDERSON JR COLLEGE PARK MD 20742

NO. OF COPIES	ORGANIZATION
1	UNIV OF TEXAS DEPT OF AEROSPACE ENG MECH ATTN DR D S DOLLING AUSTIN TX 78712-1055
	ABERDEEN PROVING GROUND
2	DIRECTOR US ARMY RSCH LABORATORY ATTN AMSRL CI LP (TECH LIB) BLDG 305 APG AA
1	DIRECTOR US ARMY RSCH LABORATORY ATTN AMSRL WM J SMITH BLDG 4600
2	DIRECTOR US ARMY RSCH LABORATORY ATTN AMSRL WM B A HORST W CIEPIELA BLDG 4600
2	DIRECTOR US ARMY RSCH LABORATORY ATTN AMSRL WM BA D LYON T BROWN BLDG 4600
1	DIR USARL ATTN AMSRL WM BD B FORCH BLDG 4600
1	DIR USARL ATTN AMSRL WM BD M NUSCA BLDG 390
10	DIR USARL ATTN AMSRL WM BC P PLOSTINS J DESPIRITO B GUIDOS K HEAVEY J SAHU (5 CYS) P WEINACHT BLDG 390
2	DIR USARL ATTN AMSRL WM BF H EDGE J LACETERA BLDG 390
1	DIR USARL ATTN AMSRL SL BE A MIKHAIL BLDG 328

NO. OF COPIES	ORGANIZATION
3	DIR USARL ATTN AMSRL CI C NIETUBICZ R NOACK J BENEK BLDG 328
3	CDR US ARMY ARDEC FIRING TABLES BRANCH ATTN R LIESKE R EITMILLER F MIRABELLE BLDG 120

INTENTIONALLY LEFT BLANK

REPORT DOCUMENTATION PAGE

Form Approved
OMB No. 0704-0188

Public reporting burden for this collection of information is estimated to average 1 hour per response, including the time for reviewing instructions, searching existing data sources, gathering and maintaining the data needed, and completing and reviewing the collection of information. Send comments regarding this burden estimate or any other aspect of this collection of information, including suggestions for reducing this burden, to Washington Headquarters Services, Directorate for Information Operations and Reports, 1215 Jefferson Davis Highway, Suite 1204, Arlington, VA 22202-4302, and to the Office of Management and Budget, Paperwork Reduction Project (0704-0188), Washington, DC 20503.

1. AGENCY USE ONLY *(Leave blank)*	2. REPORT DATE	3. REPORT TYPE AND DATES COVERED
	December 2001	Final

4. TITLE AND SUBTITLE	5. FUNDING NUMBERS
Numerical Computations of Supersonic Flow Over Elliptical Projectiles	PR: 1L162618AH80
6. AUTHOR(S) Sahu, J.; Heavey, K.R.; Edge, H.L. (all of ARL)	
7. PERFORMING ORGANIZATION NAME(S) AND ADDRESS(ES) U.S. Army Research Laboratory Weapons & Materials Research Directorate Aberdeen Proving Ground, MD 21005-5066	8. PERFORMING ORGANIZATION REPORT NUMBER
9. SPONSORING/MONITORING AGENCY NAME(S) AND ADDRESS(ES) U.S. Army Research Laboratory Weapons & Materials Research Directorate Aberdeen Proving Ground, MD 21005-5066	10. SPONSORING/MONITORING AGENCY REPORT NUMBER ARL-TR-2589
11. SUPPLEMENTARY NOTES	
12a. DISTRIBUTION/AVAILABILITY STATEMENT Approved for public release; distribution is unlimited.	12b. DISTRIBUTION CODE

13. ABSTRACT *(Maximum 200 words)*

Computational fluid dynamics (CFD) approaches were used to compute the supersonic and hypersonic flow fields and aerodynamic forces and moments on elliptical projectiles. Steady state numerical results have been obtained at several supersonic Mach numbers between 2.5 and 4.0 and several angles of attack from 0 to 12 degrees for the "jet-off" conditions with the use of Euler and Navier-Stokes flow solvers. In addition, numerical computations have been performed for the "jet-on" conditions to study the interaction of a helium jet with a free stream Mach 4.0 flow. In general, very good agreement of the computed aerodynamic coefficients with the experimental data was achieved at all speeds and angles of attack investigated for jet-off conditions. A small discrepancy exists in the comparisons for the axial force. CFD results for the jet-on case show the qualitative features and strong flow interaction between the jet and the free stream flow. The results show the predictive capabilities of CFD techniques for supersonic flow over elliptical projectiles.

14. SUBJECT TERMS			15. NUMBER OF PAGES
aerodynamic coefficient angle of attack	computational fluid dynamics elliptical projectile	hypervelocity jet flow	45
			16. PRICE CODE

17. SECURITY CLASSIFICATION OF REPORT	18. SECURITY CLASSIFICATION OF THIS PAGE	19. SECURITY CLASSIFICATION OF ABSTRACT	20. LIMITATION OF ABSTRACT
Unclassified	Unclassified	Unclassified	

NSN 7540-01-280-5500

Standard Form 298 (Rev. 2-89)
Prescribed by ANSI Std. Z39-18
298-102